Structures 72 (2025) 108206

Contents lists available at ScienceDirect

Structures

journal homepage: www.elsevier.com/locate/structures

Utilization of numerical and machine learning to predict the monotonic compressive response of square double-skin tubular columns (SDSTC)

Yang Ren [a], Haytham F. Isleem [b,c,*], Ali Jahami [d], Rupesh Kumar Tipu [e]

[a] Master of Computer Science, City University of Seattle, Seattle 98102, United States
[b] Jadara University Research Center, Jadara University, Irbid 21110, Jordan
[c] Department of Computer Science, University of York, York YO10 5DD, United Kingdom
[d] Faculty of Engineering, University of Balamand, P.O. Box 100, Tripoli, Lebanon
[e] School of Engineering & Technology, K. R. Mangalam University, Gurugram, Haryana 122103, India

ARTICLE INFO

Keywords:
Double-skin tubular columns
Fiber reinforced polymer
Numerical analysis
Artificial Intelligence
Stress-strain behavior
Monotonic loading

ABSTRACT

The comprehensive study embarks on an interdisciplinary approach, merging the rigorous analysis of numerical simulations with the predictive capabilities of Artificial Intelligence (AI), to investigate the behavior of double-skin tubular columns (DSTCs) under monotonic loading conditions. This research stands at the intersection of traditional structural engineering and modern computational techniques, aiming to unravel the complexities associated with the stress-strain responses of DSTC columns. By leveraging advanced AI models, the study not only enhances the accuracy of predictions in scenarios laden with complex variables but also significantly contributes to the optimization of structural systems. Compared to other ML approaches, Adam-Boosted Gradient boosting regression exhibited the best performance metrics with R^2 and RMSE of 0.993 and 51.20 kN and 1 and 4.70685E-18 for load carrying capacity and ultimate strain capacity, respectively. The implications of this integration are profound, offering pathways to more resilient, efficient, and sustainable construction methodologies. The detailed understanding gained from this research provides a solid foundation for future explorations into the use of FRP materials in construction, paving the way for a new era of engineering solutions that harmonize strength, durability, and environmental stewardship.

1. Introduction

The study of Double Skin Tubular Columns (DSTCs) is critically important, particularly in high-rise buildings and offshore platforms, where achieving a high strength-to-weight ratio and resilience against extreme environmental conditions are paramount. Research demonstrates that adopting appropriate construction solutions significantly enhances the resilience of high-rise buildings to dynamic loadings, including explosions, through the use of reinforced concrete and advanced simulation techniques [1]. Furthermore, enhanced seismic structural systems, such as friction pendulum bearings and seismic isolation, are effective in achieving strength-to-weight resilience, ensuring continued operation and safeguarding investments in high-risk areas [2]. Additionally, evaluation metrics for seismic resilience have shown that improving the performance of nonstructural components, such as partition walls and ceilings, can significantly bolster the overall resilience of high-rise structures [3].

Many studies have been conducted on the structural mechanics and influencing factors for DSTCs [4–7]. Fanggi and Ozbakkaloglu [4] investigated how the diameter and thickness of the inner steel tube significantly influence the compressive behavior of FRP-HSC-steel DSTCs, demonstrating that larger diameters and thicknesses enhance ultimate axial stress and strain by improving confinement effects. Xiong et al. [5] performed a comparative analysis of the compressive behavior

Abbreviations: AI, Artificial Intelligence; BP-ANN, Backpropagation Artificial Neural Network; BR, Bagging Regressor; CDP, Concrete Damage Plasticity; CFRP, Carbon Fiber Reinforced Polymer; CFDST, Concrete-Filled Double-Skin Tubular; CFFT, Concrete-Filled FRP Tube; DTR, Decision Tree Regressor; DCFSST, Double-Skin Concrete-Filled Stainless Steel Tubular Columns; DSTC, Double-Skin Tubular Columns; ETR, Extra Tree Regression; FEM, Finite Element Modeling; FRP, Fiber Reinforced Polymer; KGE, Kling-Gupta Efficiency; ML, Machine Learning; MSE, Mean Squared Error; RF, Random Forest; SVR, Support Vector Regressor; RAE, Relative Absolute Error; REC, Regression Error Characteristics; RMSE, Root Mean Square Error; MAE, Mean Absolute Error; MAPE, Mean Absolute Percentage Error; SHAP, Shapley Additive Explanations; VAF, Variance Account Factor; GBRt, Gradient Boosting Tree.

* Corresponding author at: Jadara University Research Center, Jadara University, Irbid 21110, Jordan.

https://doi.org/10.1016/j.istruc.2025.108206
Received 11 August 2024; Received in revised form 23 November 2024; Accepted 6 January 2025
2352-0124/© 2025 Institution of Structural Engineers. Published by Elsevier Ltd. All rights are reserved, including those for text and data mining, AI training, and similar technologies.

of FRP-concrete-steel DSTCs, highlighting variations in failure mechanisms and axial stiffness relative to other column types, which is essential for optimizing DSTC performance in various structural applications. Additional studies demonstrate that cyclic loading can further enhance the strength and strain ratios in concrete within DSTCs, as noted by Fanggi and Ozbakkaloglu [6]. They observed that hollow DSTCs exhibit greater strength enhancements under cyclic loading compared to monotonic loading, while filled DSTCs also show increased strength ratios, underscoring the importance of loading conditions in DSTC design for high-stress applications. Further research into FRP-HSC-steel DSTCs shows that FRP provides added confinement, improving performance under cyclic loads, which is crucial for resilience in seismic or high-impact environments [7]. These studies collectively provide a comprehensive basis for developing optimized DSTC configurations that meet the unique demands of modern engineering applications.

Other studies have focused on enhancements through material innovations in DSTCs [8–11]. Farahi et al. [8] explored the use of corrugated plates in concrete-filled double-skin tubular (CFDST) columns, revealing significant improvements in ductility and energy absorption. Wan et al. [9] investigated the reinforcement of CFDST columns with carbon fiber reinforced polymer (CFRP), introducing a novel design formula that optimizes performance under axial loads. Recent advancements have also focused on integrating innovative reinforcement materials like fiber-reinforced composites and hybrid structures. Huang et al. [10] demonstrated that hybrid composites incorporating carbon and glass fibers, enhanced with nano copper oxide particles, significantly improve mechanical properties, making them highly suitable for load-bearing applications. Additionally, Zou et al. [11] presented a novel rolling strategy using corrugated structures in carbon fiber/aluminum composites, achieving notable increases in tensile and bending strength, which are essential for high-stress environments like offshore platforms. These material innovations contribute to enhancing the structural resilience and energy absorption capacities of DSTCs, addressing the rigorous demands of modern engineering applications.

In exploring the realms of fire resistance and seismic resilience for DSTCs, Mohd Zuki et al. [12] examined the performance of concrete-filled double-skin tubular (CFDST) columns under high temperatures, identifying reductions in strength and stiffness due to fire exposure. Zhang et al. [13] conducted experimental studies on hybrid DSTCs subjected to axial compression and cyclic lateral loading, demonstrating their remarkable ductility and robust seismic resistance, crucial for earthquake-prone regions. Additional studies further emphasize the importance of fire-resistant designs in high-performance structures. Dwaikat and Kodur [14] demonstrated that fire exposure significantly affects the load-bearing capacity of restrained concrete beams, with high-strength concrete beams showing lower fire resistance and higher spalling rates due to reduced permeability. Furthermore, Hashemi et al. [15] introduced a seismic-resilient system using laminated timber panels with Resilient Slip Friction joints, showcasing superior ductility, energy dissipation, and self-centering behavior compared to conventional systems, thus advancing earthquake-resilient construction practices. These additional studies provide broader insights into DSTC applications and the integration of innovative materials for enhanced resilience.

In the sphere of design and modelling approaches for DSTCs, Patel et al. [16] made significant strides by developing a comprehensive computational model specifically for short double-skin concrete-filled stainless steel tubular (CFDSST) columns, which effectively assesses the impact of geometric configurations and material strengths. Complementing this, Liang [17] introduced a sophisticated mathematical model that accurately characterizes the axial load-deflection performance of high-strength circular CFDST slender columns under eccentric loading, offering an efficient approach for both computational analysis and design purposes. Similar studies can be found in the literature on design and modelling approaches for DSTCs [18,19].

Some studies focused on alternative materials and sustainability for DSTCs [20–23]. Youssf et al. [20] delved into the utilization of Rubcrete in hybrid DSTCs, underscoring the material's ability to enhance axial and hoop strain capacities, particularly when using fine rubber particles. Complementing this, Ali and Salman [21] investigated how the void ratio of the inner steel tube influences the compression behavior of hybrid DSTCs, discovering a notable improvement in the stress-strain behavior of concrete within these structures. These studies point towards innovative approaches in materials usage, contributing to the sustainability and performance of DSTCs.

Moreover, some studies focused on unique structural configurations of DSTCs [24–27]. Chen et al. [24] conducted a thorough investigation into the behavior of thin-walled dodecagonal section double skin concrete-filled steel tubular beam-columns, employing finite element modeling to analyze their structural responses. Additionally, Guo et al. [25] focused on square CFDST short columns with double internal steel tubes, leading to the development of simplified formulae for accurately estimating the ultimate strength of these columns. Recent studies have explored even more unconventional designs, such as circular and cruciform cross-sections, which enhance both load-bearing capacity and resilience under seismic loading. For example, Kim et al. [26] examined the fire resistance of composite columns with circular and rectangular configurations, finding that clamped-end circular sections exhibit extended fire resistance. These studies collectively enhance the understanding of DSTC structural behavior in less conventional configurations, expanding the possibilities for specialized applications.

Recent advancements in machine learning (ML) have significantly impacted the field of structural engineering, particularly in performance prediction and optimization [28–33]. Hong et al. [34] utilized ML techniques to predict the fire resistance of concrete-filled double-skin tubular (CFDST) columns, demonstrating improved prediction accuracy for complex non-linear problems. Similarly, Nguyen et al. [35] explored the application of gradient boosting regression (GBR) and XGBoost models for predicting compressive and tensile strengths of concrete, achieving high efficiency in performance prediction. Stergiou et al. [36] highlighted the use of ML for enhancing material property prediction and process optimization, such as thermal and mechanical properties of structural materials, which leads to improved material performance in engineering applications. These advancements not only optimize structural design processes but also enable rapid assessments of complex structural systems, making ML an indispensable tool in modern engineering.

Nguyen and Ly [37] explored similar concepts, focusing on the application of ML in predicting the behavior of CFDST columns under various loading conditions. Their research underscores the potential of ML algorithms in enhancing the accuracy and efficiency of structural analysis in engineering. Furthermore, Wu et al. [38] extended these studies by integrating ML into traditional engineering approaches like the Rankine method. They modified the Rankine method to include ML predictions, resulting in a more accurate and reliable approach for analyzing CFDST columns under fire attacks.

Recent research on DSTCs has not only significantly advanced our understanding of their behavior, design, and application in various contexts but also underscored the transformative role of machine learning in structural engineering. Innovations in materials and modeling techniques, including the integration of ML algorithms with traditional engineering methods, have greatly enhanced the structural performance of DSTCs. This is evident in their improved strength, ductility, and resilience to environmental challenges. Moreover, the application of ML in the analysis and prediction of DSTCs behavior under varied conditions is a testament to its potential in elevating accuracy and efficiency in structural analysis and design. The ongoing exploration of new configurations and materials, coupled with the advancements in machine learning, heralds a promising future for DSTCs in diverse engineering applications.

2. Research Significance

This research combines numerical analysis with AI generative modeling to comprehensively investigate the effects of various parameters on fiber reinforced polymer (FRP) column behavior under monotonic loading conditions. Numerical analysis is employed to simulate the stress-strain behavior under different scenarios, yielding detailed insights. AI generative models enhance this exploration by predicting responses across a wide range of parameters, particularly in complex situations that are challenging to simulate directly. The study significantly advances the understanding of FRP column behavior, providing valuable insights for engineers, designers, and researchers. A deeper comprehension of these parameters facilitates the development of optimized structural systems that incorporate FRP columns, promoting safer, more efficient, and sustainable construction practices. The subsequent sections will present a thorough review of related literature, outline the methodology used, and delve into the individual effects of key parameters, leading to important conclusions and practical applications in structural engineering. Fig. 1 illustrates the research's methodology in a graphic format.

3. Analysis program

3.1. Experimental work

This study is grounded on the findings of two pivotal articles in the field of FRP concrete-steel hybrid structures. The first, by Fanggi and Ozbakkaloglu [39], presents an experimental study exploring the compressive behavior of square FRP-concrete composite columns. This study involved testing 40 column specimens, which included 24 FRP-concrete-steel DSTCs, four concrete-filled FRP tubes (CFFTs), and 12 CFFTs with inner voids (H-CFFTs). Key parameters such as the concrete's strength, the cross-sectional shape, and the dimensions of the inner steel tube were investigated. The study found that DSTCs with circular inner steel tubes displayed increased ultimate axial stress but reduced ultimate axial strain when compared to DSTCs with hollow inner steel tubes. Additionally, concrete in hollow DSTCs with square inner steel tubes developed significantly lower ultimate axial stresses and strains than their circular counterparts. However, the performance of these specimens improved dramatically when the square inner steel tube was filled with concrete.

The second article, by Yu and Teng [40], extends research on circular

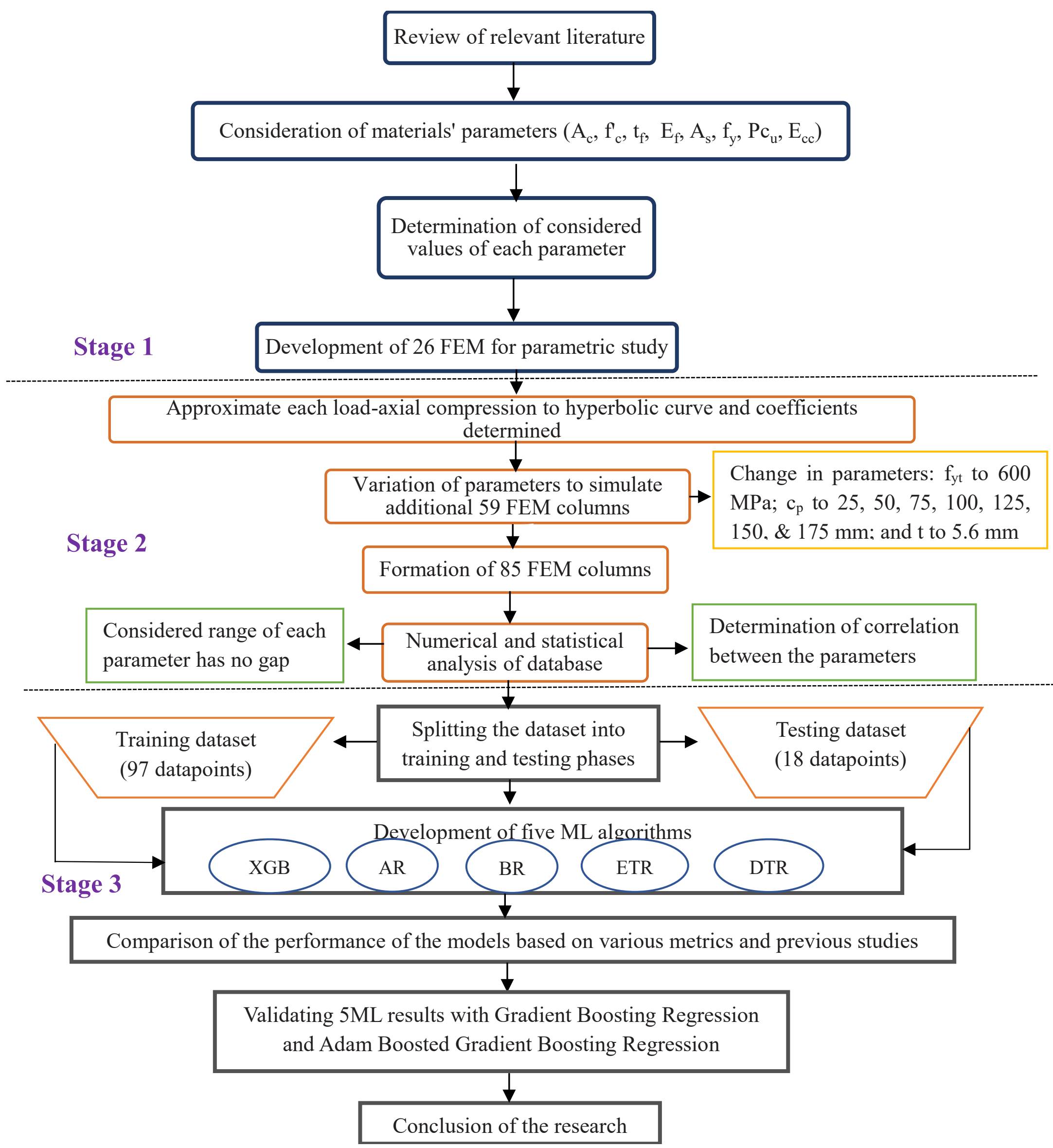

Fig. 1. Flowchart that briefly shows the process of the research methodology.

hybrid DSTCs to square hybrid DSTCs, where the outer FRP tube is square while maintaining a circular inner steel tube. This paper focused on the compressive behavior of these square hybrid DSTCs, using FRP tubes formed through a wet-layup process. The results demonstrated that the concrete in these square hybrid DSTCs is effectively confined by the two tubes, exhibiting behavior similar to that of concrete in FRP-confined solid columns. The study also proposed a stress-strain model for concrete in square hybrid DSTCs, which was shown to provide reasonably accurate predictions of the test results.

Table 1 provides a comprehensive summary of the specimens utilized in the experimental studies conducted by Fanggi and Ozbakkaloglu [39], as well as Yu and Teng [40]. It details the dimensions and characteristics of the external columns, which measured 150 × 150 mm. The internal hole diameter (di) varied between 60.3 mm and 114.5 mm, while the thickness of the tubes (ts) ranged from 3.2 mm to 6 mm. The mechanical properties of the steel tubes are meticulously cataloged in the table, highlighting both the yield strength (fy) and the ultimate strength (fu). Furthermore, the table delineates the compressive strength of the concrete (f'c). For an in-depth understanding of the experimental methodologies employed in this study, additional specifics are systematically documented in Table 1.

Our current study leverages these findings to conduct a parametric study using finite element modeling and machine learning (Fig. 2). These references provide a foundational understanding of the behavior of hybrid FRP-concrete-steel structures under compressive loads, informing the development and validation of our computational models and machine learning algorithms.

3.2. Parametric study

The parametric study was meticulously structured, building upon the foundational experimental work previously outlined. This study rigorously examined various influential factors: the number of FRP layers, the geometric shape of the steel tube, the arrangement patterns of the steel tubes, as well as the variance in steel tube thickness, diameter, and yield strength. Table 2 shows the details of the specimens considered in the parametric study.

To systematically explore these variables, six distinct groups were delineated for in-depth analysis:

1. Group G2 paralleled Group G1 but incorporated modifications, specifically a reduction in concrete strength and the number of FRP layers.
2. Group G3 was designed akin to Group G1 specimens but was distinct in its inclusion of an additional steel tube, configured as a double layer with a diameter constituting half that of the original.
3. Group G4, while bearing resemblance to Group G1 specimens, distinguished itself by enhancing the strength of the steel tube.
4. Group G5 mirrored Group G2, albeit with an altered steel strength for the tubes.
5. Group G6 emulated Group G3, yet differentiated itself by varying the steel tube strength.
6. Group G7, while fundamentally similar to the other groups, was uniquely characterized by its distinct concrete strength, steel tube dimensions, and number of FRP layers.

The intent of these methodically structured groups is to harness the capabilities of finite element modeling. This strategic approach aims to not only derive insightful findings from the modeling but also to leverage these results to enrich machine learning analyses. The ultimate goal is to cultivate a comprehensive understanding of the stress-strain behavior inherent to DSTC, thereby advancing the knowledge frontier in this domain.

4. Numerical Validation

4.1. General

Finite element modeling (FEM) is a cornerstone in the field of structural engineering, serving as a pivotal tool for understanding and predicting the behavior of structures under various loads and conditions. This computational technique breaks down complex structures into smaller, manageable elements, allowing engineers to scrutinize the response of materials and designs to stress, vibration, heat, and other physical effects. FEM's precision and adaptability make it indispensable for simulating real-world scenarios, optimizing designs, and ensuring the safety and efficiency of structures. By providing a detailed insight into structural performance, FEM aids in the innovation of construction methods and the advancement of materials science, marking its significance as an integral component in the evolution and resilience of modern infrastructure.

ABAQUS, a sophisticated finite element modeling software, has gained substantial importance in the realm of structural engineering, primarily due to its robust capabilities in simulating and analyzing complex structural behaviors. Recent studies highlight its crucial role in various applications. For instance, Mushthofa et al. [41] emphasized the significance of ABAQUS in ensuring the structural integrity and functionality of critical systems through precise estimations in steel welding processes. Bongiovì et al. [42] showcased the software's utility in conducting thermal and structural analyses, particularly in evaluating the structural design criteria of European water-cooled lithium lead breeding blankets. Xie et al. [43] demonstrated the application of

Table 1
Specimens considered by Fanggi and Ozbakkaloglu [39] and Yu and Teng [40].

Ref. No.	*Code*	*Group*	*Inner Section*	*Steel Tube Arrangement*	*di (mm)*	*ts (mm)*	*FRP Type*	*No. Layers*	*f'c (Mpa)*	*fy (Mpa)*	*fu (Mpa)*
[39]	DSTC−1&2	G1	Circular Hollow DSTC	Single	60.3	3.6	AFRP	8	98.2	319	384
	DSTC−3&4		Circular Filled DSTC		60.3	3.6		8	98.2	319	384
	DSTC−5&6		Circular Hollow DSTC		88.9	3.2		8	98.2	320	404
	DSTC−7&8		Circular Filled DSTC		88.9	3.2		8	98.2	320	404
	DSTC−9&10		Circular Hollow DSTC		114.3	6.0		8	98.2	449	524
	DSTC−11&12		Circular Filled DSTC		114.3	6.0		8	98.2	449	524
	DSTC−13&14		Circular Hollow DSTC		88.9	3.2		3	47.0	320	404
	DSTC−15&16		Circular Filled DSTC		88.9	3.2		3	47.0	320	404
	DSTC−17&18		Square Hollow DSTC		89.0	3.5		8	98.2	462	492
	DSTC−19&20		Square Filled DSTC		89.0	3.5		8	98.2	462	492
	DSTC−21&22		Square Hollow DSTC		89.0	3.5		3	47.0	462	492
	DSTC−23&24		Square Filled DSTC		89.0	3.5		3	47.0	462	492
	CFFT−1&2		Filled - No Steel Tube	-	0	0		8	98.2	0	0
	CFFT−3&4		Filled - No Steel Tube		0	0		3	47.0	0	0
[40]	D37-A2-I&II		Circular Hollow DSTC	Single	76.3	3.3	GFRP	2	37.0	364	433
	D37-A3-I&II		Circular Hollow DSTC		76.3	3.3		3	37.0	364	433
	D37-B2-I&II		Circular Hollow DSTC		114.5	5.2		2	37.0	382	427
	D37-B3-I&II		Circular Hollow DSTC		114.5	5.2		3	37.0	382	427

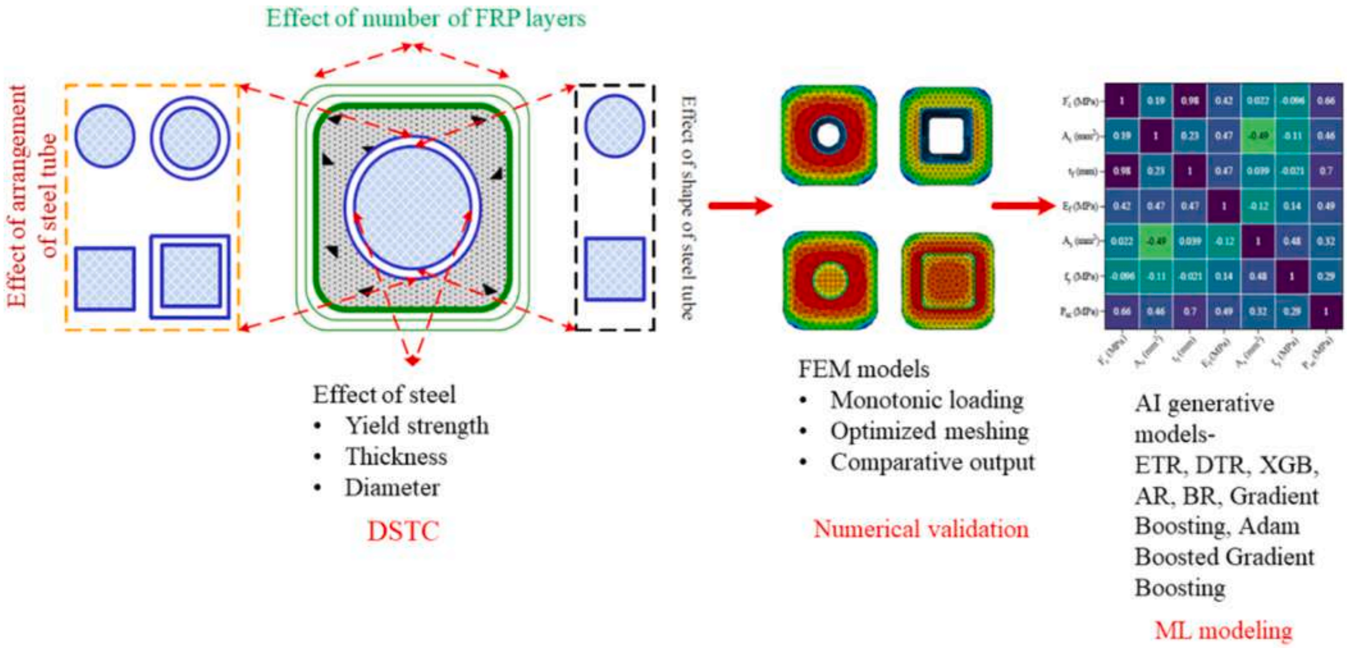

Fig. 2. Illustrative diagram of the analytical approach proposed in study.

ABAQUS in evaluating the safety of undersea structures by establishing a method for large-deformation simulation of submarine landslides. Zhang et al. [44] relied on ABAQUS for fatigue life prediction in steel spiral cases of pumped-storage power plants, highlighting its contribution to the field of structural engineering. Lastly, Abramowicz et al. [45] utilized ABAQUS for modeling sustainable laminated veneer lumber slabs, underscoring its vital role in ensuring the safe operation of civil engineering structures. These studies collectively reinforce the indispensability of ABAQUS in tackling complex structural challenges, proving it to be an integral tool in the structural engineering domain.

4.2. Model properties

In the parametric analysis undertaken, each case was meticulously modeled using ABAQUS software. The modeling primarily focused on three fundamental components: the concrete body, steel tubes, and FRP composites, each simulated with distinct element types to best represent their physical and mechanical properties (Fig. 3).

The concrete body was modeled as C3D6 elements, representing a 6-node linear triangular prism. This element type is specifically chosen for its ability to accurately simulate the nonlinear, inelastic behavior of concrete under load, as well as its capacity to handle complex load applications and boundary conditions.

The steel tubes, critical for providing structural rigidity and stability, were modeled using C3D8R elements. These 8-node linear brick elements, with reduced integration and hourglass control, are adept at capturing the behavior of steel structures, especially under the conditions of linear elasticity and plasticity, which are paramount in structural analysis and design.

For the FRP components, S4R elements were employed. These 4-node, quadrilateral, stress/displacement shell elements are particularly suited for modeling thin shell structures like FRP composites. The reduced integration and large-strain formulation of S4R elements allow for an accurate representation of the FRP's mechanical behavior, especially under high strain conditions, ensuring a realistic simulation of the material's performance.

The interaction between these constituent parts was meticulously defined using various constraints to simulate the physical behavior of the interface areas accurately. The interface between the concrete and the FRP, as well as between the concrete and steel tubes, was modeled using the surface-to-surface tie constraint. This constraint was meticulously defined to include both tangential and normal behavior, offering a comprehensive simulation of the interface interactions. The normal behavior was designated as "hard," ensuring a perfectly bonded interaction, while the tangential behavior was modeled using the "penalty" method, with a friction coefficient of 0.2, to accurately simulate the frictional forces at play.

Additionally, the extremities of the specimen, namely the start and end faces, were assigned a coupling constraint. This constraint was rigorously defined to restrict all degrees of freedom, thereby simulating a realistic boundary condition that these faces would encounter in practical scenarios.

The approach adopted in this study is in alignment with recent advancements and methodologies in the field, as detailed in contemporary literature. These references not only validate the modeling techniques and element choices employed but also provide a comparative framework for assessing the predictive accuracy and reliability of the simulation results.

4.3. Material models

The concrete damage plasticity (CDP) model in Abaqus was adopted in this research to model concrete material. This model is recognized for its capability to simulate the inelastic behavior of concrete, is a robust tool underpinned by the principles of continuum damage mechanics and plasticity theory. This model provides a comprehensive framework for analyzing the intricate responses of concrete under diverse loading conditions, including uniaxial load, shear load, seismic loads, and impact loads. Its utility extends to the examination of complex structures, notably reinforced concrete elements, which are often subjected to seismic loading or other dynamic forces. The CDP model's versatility and detailed approach make it an indispensable tool in the simulation and analysis of concrete's behavior under various stress conditions [46–48], thereby contributing significantly to the field of structural engineering and design. Table 3 summarizes the parameters adopted for defining each concrete grade used in the parametric study.

The material properties of the steel tubes were characterized by an elastoplastic material model. This model delineates that the steel

Table 2
Parametric study details.

Code	*Group*	*Inner Section*	*Steel Tube Arrangement*	*di (mm)*	*ts (mm)*	*FRP Type*	*No. Layers*	*f'c (Mpa)*	*fy (Mpa)*	*fu (Mpa)*
DSTC−1&2	G2	Circular Hollow DSTC	Single	60.30	3.60	AFRP	3	36.8	319	384
DSTC−3&4		Circular Filled DSTC		60.30	3.60		3	36.8	319	384
DSTC−5&6		Circular Hollow DSTC		88.90	3.20		3	36.8	320	404
DSTC−7&8		Circular Filled DSTC		88.90	3.20		3	36.8	320	404
DSTC−9&10		Circular Hollow DSTC		114.30	6.02		3	36.8	449	524
DSTC−11&12		Circular Filled DSTC		114.30	6.02		3	36.8	449	524
DSTC−17&18		Square Hollow DSTC		89.00	3.50		3	36.8	462	492
DSTC−19&20		Square Filled DSTC		89.00	3.50		3	36.8	462	492
D37-A4		Circular Hollow DSTC		76.30	3.30	GFRP	4	37.0	364.3	433.1
D37-B4		Circular Hollow DSTC		114.50	5.20		4	37.0	381.7	426.9
DSTC−3&4	G3	Circular Filled DSTC	Double	60.30	3.60	AFRP	8	98.2	319	384
DSTC−7&8		Circular Filled DSTC		88.90	3.20		8	98.2	320	404
DSTC−11&12		Circular Filled DSTC		114.30	6.02		8	98.2	449	524
DSTC−19&20		Square Filled DSTC		89.00	3.50		8	98.2	462	492
DSTC−1&2	G4	Circular Hollow DSTC	Single	60.30	3.60		8	98.2	667.5	827
DSTC−3&4		Circular Filled DSTC		60.30	3.60		8	98.2	667.5	827
DSTC−5&6		Circular Hollow DSTC		88.90	3.20		8	98.2	667.5	827
DSTC−7&8		Circular Filled DSTC		88.90	3.20		8	98.2	667.5	827
DSTC−9&10		Circular Hollow DSTC		114.30	6.02		8	98.2	667.5	827
DSTC−11&12		Circular Filled DSTC		114.30	6.02		8	98.2	667.5	827
DSTC−13&14		Circular Hollow DSTC		88.90	3.20		3	47.0	667.5	827
DSTC−15&16		Circular Filled DSTC		88.90	3.20		3	47.0	667.5	827
DSTC−17&18		Square Hollow DSTC		89.00	3.50		8	98.2	667.5	827
DSTC−19&20		Square Filled DSTC		89.00	3.50		8	98.2	667.5	827
DSTC−21&22		Square Hollow DSTC		89.00	3.50		3	47.0	667.5	827
DSTC−23&24		Square Filled DSTC		89.00	3.50		3	47.0	667.5	827
DSTC−1&2	G5	Circular Hollow DSTC	Single	60.30	3.60		3	36.8	667.5	827
DSTC−3&4		Circular Filled DSTC		60.30	3.60		3	36.8	667.5	827
DSTC−5&6		Circular Hollow DSTC		88.90	3.20		3	36.8	667.5	827
DSTC−7&8		Circular Filled DSTC		88.90	3.20		3	36.8	667.5	827
DSTC−9&10		Circular Hollow DSTC		114.30	6.02		3	36.8	667.5	827
DSTC−11&12		Circular Filled DSTC		114.30	6.02		3	36.8	667.5	827
DSTC−17&18		Square Hollow DSTC		89.00	3.50		3	36.8	667.5	827
DSTC−19&20		Square Filled DSTC		89.00	3.50		3	36.8	667.5	827
DSTC−3&4	G6	Circular Filled DSTC	Double	60.30	3.60		8	98.2	667.5	827
DSTC−7&8		Circular Filled DSTC		88.90	3.20		8	98.2	667.5	827
DSTC−11&12		Circular Filled DSTC		114.30	6.02		8	98.2	667.5	827
DSTC−19&20		Square Filled DSTC		89.00	3.50		8	98.2	667.5	827
DSTC−3&4	G7	Circular Filled DSTC	Single	60.30	3.60		4	30.0	667.5	827
DSTC−7&8		Circular Filled DSTC		88.90	3.20		4	30.0	667.5	827
DSTC−11&12		Circular Filled DSTC		114.30	6.02		4	30.0	667.5	827
DSTC−15&16		Circular Filled DSTC		88.90	3.20		2	20.0	667.5	827
DSTC−19&20		Square Filled DSTC		89.00	3.50		4	30.0	667.5	827
DSTC−23&24		Square Filled DSTC		89.00	3.50		2	20.0	667.5	827

exhibits elastic behavior up to the yield point, beyond which it transitions into plastic deformation. To accurately represent the behavior of each steel grade, a detailed assessment was conducted, incorporating multiple data points to construct the definitive stress-strain curves. Table 4 presents the primary parameters employed to define the steel material properties. In the case of the FRP materials, they were modeled as laminates, incorporating key mechanical properties such as elastic modulus, tensile strength, and ultimate tensile strain, all of which are systematically outlined in Table 5.

4.4. Loads and Boundary Conditions

A static load step, spanning a duration of 1 second, was established to delineate the applied load. To facilitate the application of concentric axial loads and the implementation of boundary conditions, two reference points were strategically positioned on opposing faces of a column. On one face, the load was allocated to the upper reference point, as depicted in Fig. 4a. Here, a displacement of 20 mm was meticulously imposed in the axial direction, concurrently constraining movements in the other directions. Conversely, on the opposing face, a comprehensive restriction was imposed on all degrees of freedom, a setup meticulously illustrated in Fig. 4b.

4.5. Meshing

In developing the ABAQUS model, a meticulous approach was undertaken to determine the optimal mesh size, culminating in the selection of a 10 mm grid. This decision was informed by a series of mesh convergence studies, which aimed to balance the dual objectives of computational efficiency and model accuracy. The chosen mesh size of 10 mm represents a compromise that ensures a sufficient level of detail to capture the critical stress and strain distributions accurately, while also keeping the computational demands within manageable limits. This balance is crucial in finite element analysis, as overly fine meshes can lead to prohibitively long computation times and excessive resource usage, while coarse meshes may overlook significant nuances in the model's behavior. Therefore, the 10 mm mesh size was strategically selected to provide a robust and reliable representation of the physical system, ensuring that the simulation results are both accurate and computationally feasible.

4.6. Simulation results

4.6.1. Comparison between experimental and FE results

Fig. 5 presents the axial load-strain curves derived from experimental investigations juxtaposed with those obtained from validated finite element models. The comparison reveals a remarkable correlation

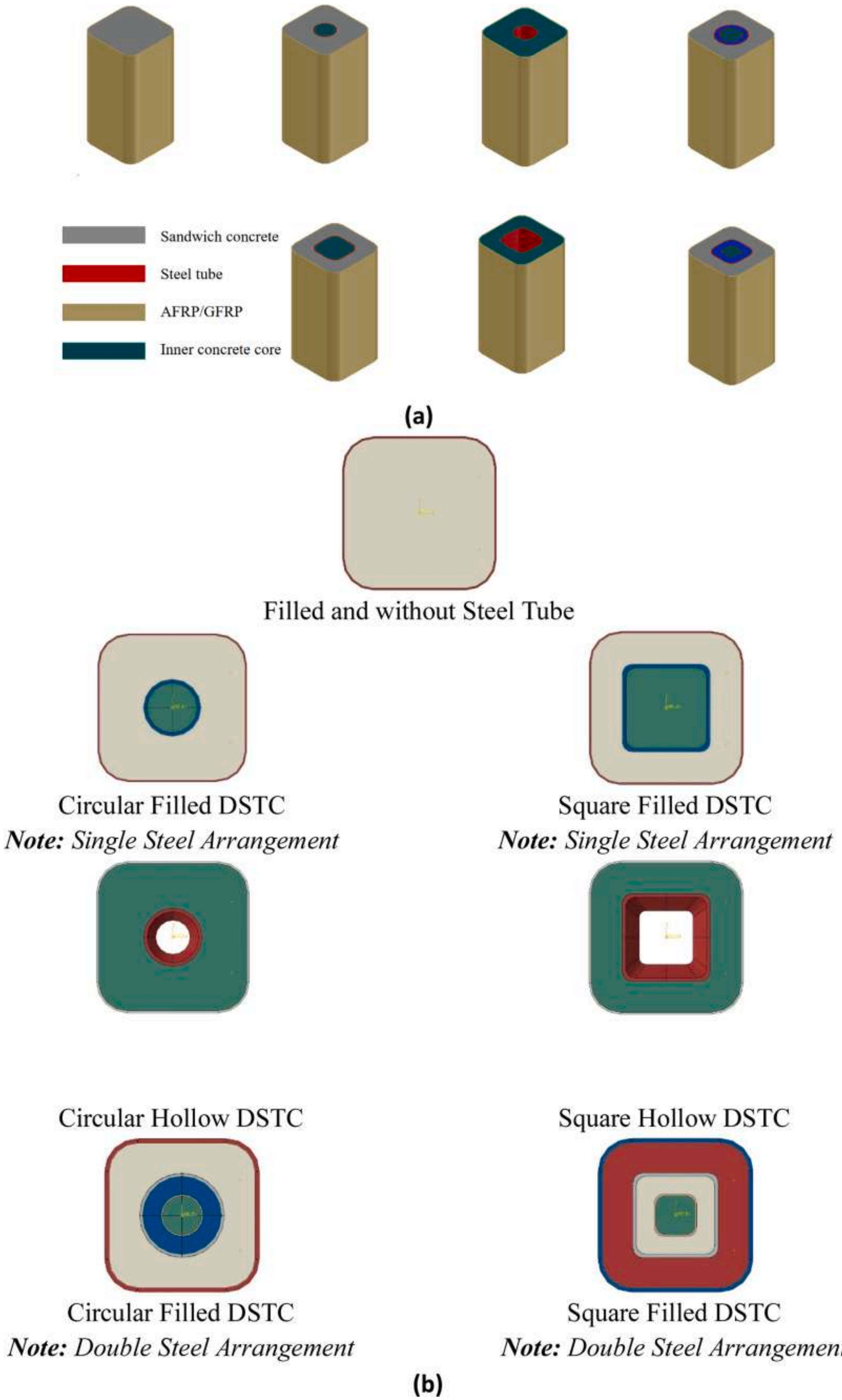

Fig. 3. Test specimens, 3D configuration of filled and hollow columns., Plan sectional view of configured columns.

Table 3
CDP parameters for concrete modeled in this study.

Parameter		*C20*	*C30*	*C36.8*	*C37*	*C47*	*C98.2*
Elasticity modulus (MPa)	E	22361	27386	30342	30414	34278	48548
Poisson's ratio	υ	0.2					
Density (kg/m^3)	ρ	2500					
Compressive strength (MPa)	f'_c	20	30	36.8	37	47	98.2
Peak Compressive strain (mm/m)	ε_c	0.00185	0.00210	0.00220	0.00221	0.00235	0.00267
Tensile Strength (MPa)	f_t	2.08	2.91	3.40	3.41	4.04	5.90
Dilation angle (°)	ψ	36					
Eccentricity	e	0.1					
Bi-axial to Uni-axial strength ratio	f_{b0}/f_{c0}	1.16					
Second stress invariant ratio	K	0.67					
Viscosity parameter	μ	0.0005					

Table 4
Input parameters for steel material modeled in this study.

Parameter		*ST319*	*ST320*	*ST449*	*ST462*	*ST364.3*	*ST381.7*	*ST667.5*
Elasticity modulus (MPa)	E	200000				206900	199000	200000
Poisson's ratio	υ	0.3						
Density (kg/m^3)	ρ	7850						
Yield Strength (MPa)	f_y	319	320	449	462	364.3	381.7	667.5
Yield Strain	ε_y	0.0015	0.0016	0.0022	0.0023	0.0018	0.0019	0.0033
Ultimate Strength (MPa)	f_u	384	404	524	492	433.1	426.9	827
Ultimate Strain	ε_u	0.0334	0.0243	0.0310	0.008	0.024	0.026	0.028

Table 5
Input parameters for FRP material modeled in this study.

Parameter		*AFRP*	*GFRP*
Elasticity Modulus (GPa)	E	128.5	95.3
Tensile strength (MPa)	f_t	2390	3055
Ultimate tensile strain	ε_c	0.0186	0.0321

between the two sets of data, evidenced by their proximity and the minimal, acceptable level of error. This congruence not only underscores the validity of the finite element models but also establishes a robust foundation for subsequent analyses. Importantly, the reliability of these models paves the way for their integration into advanced predictive frameworks, including machine learning algorithms, thereby enhancing the precision and depth of future analytical endeavors in this domain.

In a complementary manner, Fig. 6 delineates the correlation between experimental findings and finite element outcomes with respect to both peak axial load and strains at failure. It features a trend line that intersects these data points, conforming to a 45-degree line equation (y = x). This graphical representation significantly highlights the alignment of the experimental and model-predicted values. Notably, the trend line exhibits an R^2 value of 98.7 % for the ultimate axial load, indicating an exceptionally high degree of correlation. Similarly, for the ultimate axial strain, the trend line achieves an R^2 value of 94.3 %. These high R^2 values are indicative of the finite element model's robust predictive accuracy and its potential as a reliable tool in the precise extrapolation of structural behavior under load, thereby reinforcing the foundational analysis presented in Fig. 5.

4.6.2. Effect of yield strength of steel tube

In the analysis of DSTC specimens featuring single steel tubes with a yield strength of 667.5 MPa, relative to the comparative yield strengths of 319, 320, 449, and 462 MPa, it was observed that the ultimate axial load demonstrated an increase within the range of 6.4–33.3 %. Pertaining to the ultimate axial strain, variations were noted, encompassing a decrement of up to 8.2 % and an increment of up to 13.9 %, with the exception of three distinct specimens. These exceptions registered a notable reduction in strain, quantified as 31.6 %, 43.2 %, and 90.6 % respectively. This phenomenon is predominantly attributed to a reduction in ductility, correlating with an elevation in the steel grade. This correlation can be traced back to the increased percentages of carbon within the steel composition, which inversely impacts the ductility of the tubes, subsequently influencing the overall ductility of the specimens.

In contrast, specimens constructed with double steel tubes exhibited a different mechanical response. When the yield strength of these tubes was escalated from 319, 320, and 449 MPa to 667.5 MPa, there was an observed enhancement in the ultimate axial load, ranging between 12.8 % and 22.4 %. Concurrently, a marginal elevation was also recorded in the ultimate strain, delineated within a spectrum of 0.9–3.1 %. These findings imply that the addition of an extra tube to DSTC specimens did not yield a substantial improvement in ductility. For a more comprehensive understanding of these behavioral trends, reference can be made to Fig. 7, which delineates the load-strain curves pertinent to the cases scrutinized within this parametric study.

4.6.3. Effect of number of FRP layers

For the circular hollow DSTC specifications featuring a hollow diameter of 76.3 mm and a wall thickness of 3.3 mm, it was observed that augmenting the number of GFRP layers from 2 to 3 catalyzed a 17 % enhancement in the ultimate axial load. This increment escalated marginally to 18 % upon the introduction of a fourth layer, signaling a plateau in strength enhancement beyond three layers. Conversely, a notable enhancement in section ductility was recorded, with the ultimate strain surging by 60.8 % for three layers and an impressive 150.3 % for four layers.

In the case of the circular hollow DSTC variant with a larger diameter of 114.5 mm and a thickness of 5.2 mm, the impact of additional GFRP layers on the ultimate axial load was comparatively subdued, registering an increase of merely 4 % for three layers and 10.6 % for four layers. This trend suggests a diminishing return in axial load enhancement with the increase in section size, thereby reducing the efficacy of additional GFRP layers on the ultimate axial strength. However, a positive trajectory was noted in the ultimate axial strain, which witnessed an increase of 17.5 % for three layers and 60.5 % for four layers, albeit these figures fall short of the improvements observed in the smaller DSTC configuration.

For an in-depth analysis and graphical representation of these findings, reference is directed to Fig. 8. This comprehensive depiction

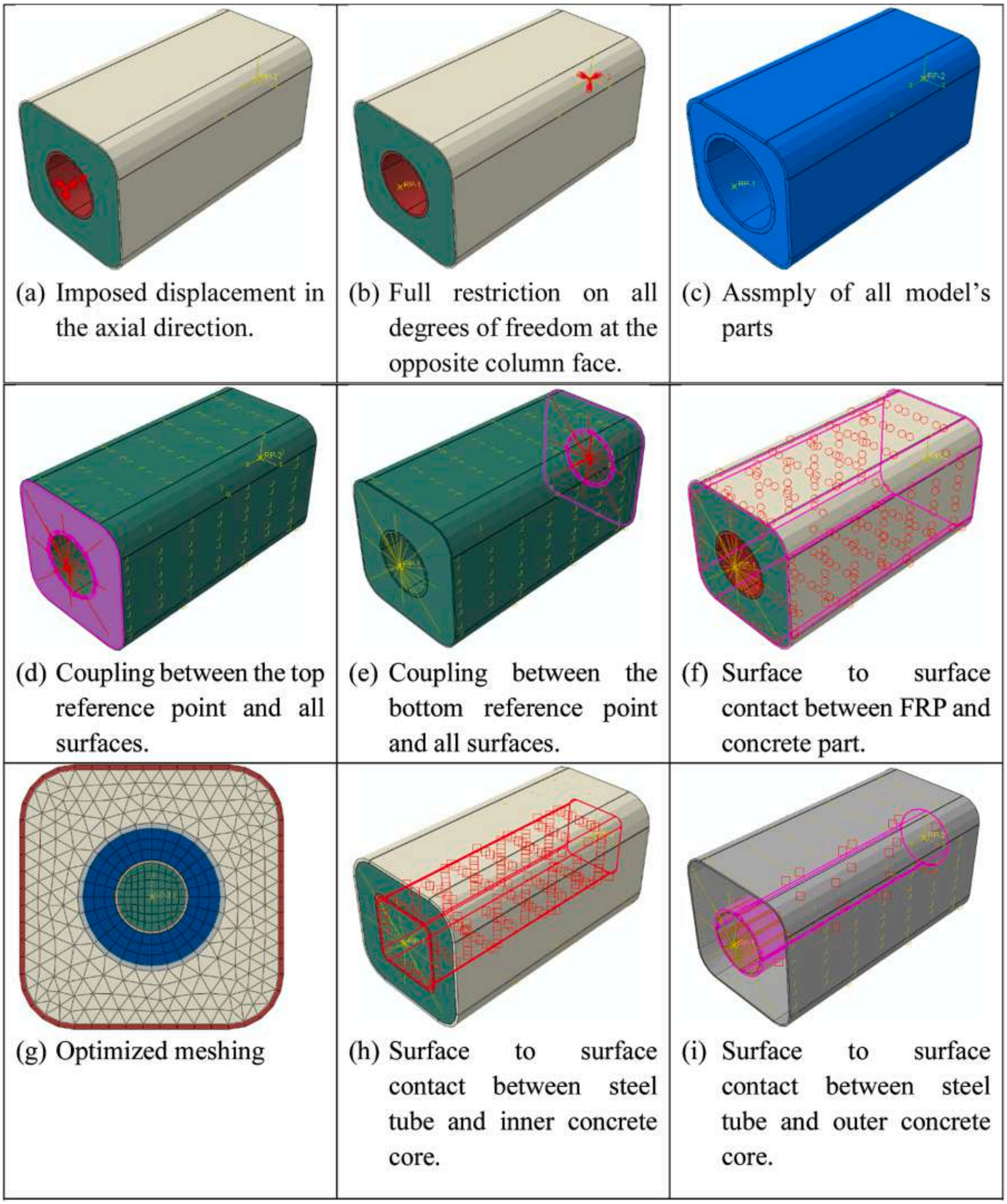

Fig. 4. Numerical model details.

elucidates the detailed interplay between the number of GFRP layers, the dimensions of the DSTC, and their collective influence on the structural properties of ultimate axial load and strain.

4.6.4. *Effect of shape of inner steel tube (i.e., Circular, Square)*

In the investigation of DSTC, the experimental outcomes for Group G1 specimens, which featured hollow tubes, revealed that DSTC specimens with circular inner steel tubes demonstrated a superior ultimate axial load capacity, surpassing their square cross-section counterparts by 10–16 %. This trend was not observed in specimens where tubes were concrete-filled. In this scenario, DSTC specimens with square inner steel tubes outperformed those with circular cross-sections, exhibiting an enhancement in ultimate axial load resistance ranging from 4.6 % to 6.3 %. Furthermore, the ultimate axial strain results indicated that hollow DSTC specimens with circular inner tubes exhibited substantially higher ultimate strains, 45–55 % greater than those with square inner tubes, signaling enhanced ductility behavior. However, this distinction in ductility was not significantly evident in concrete-filled DSTC specimens.

Group G2 specimens presented a distinct behavior pattern, particularly at lower concrete compressive strength values. Irrespective of the tubes being filled or hollow, DSTC specimens with square inner tubes consistently showed superior axial load resistance compared to those with circular inner tubes. The increase in axial load resistance was approximately 12.9 % for hollow tubes and 6.7 % for filled tubes. In terms of ultimate axial strain, square inner tubes in hollow DSTC

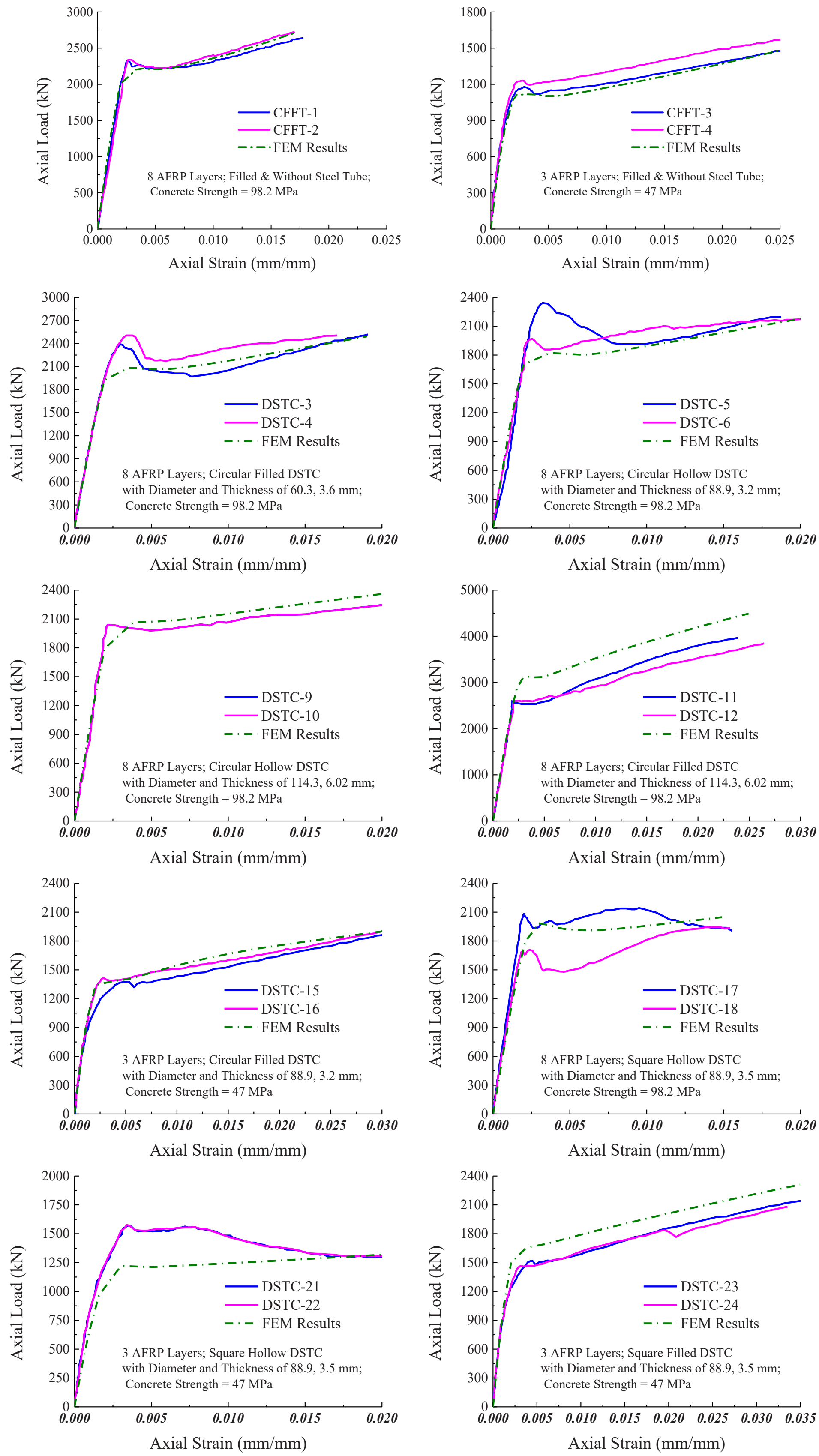

Fig. 5. Comparative analysis of axial load-strain curves: experimental data versus finite element model predictions for selected specimens in the study.

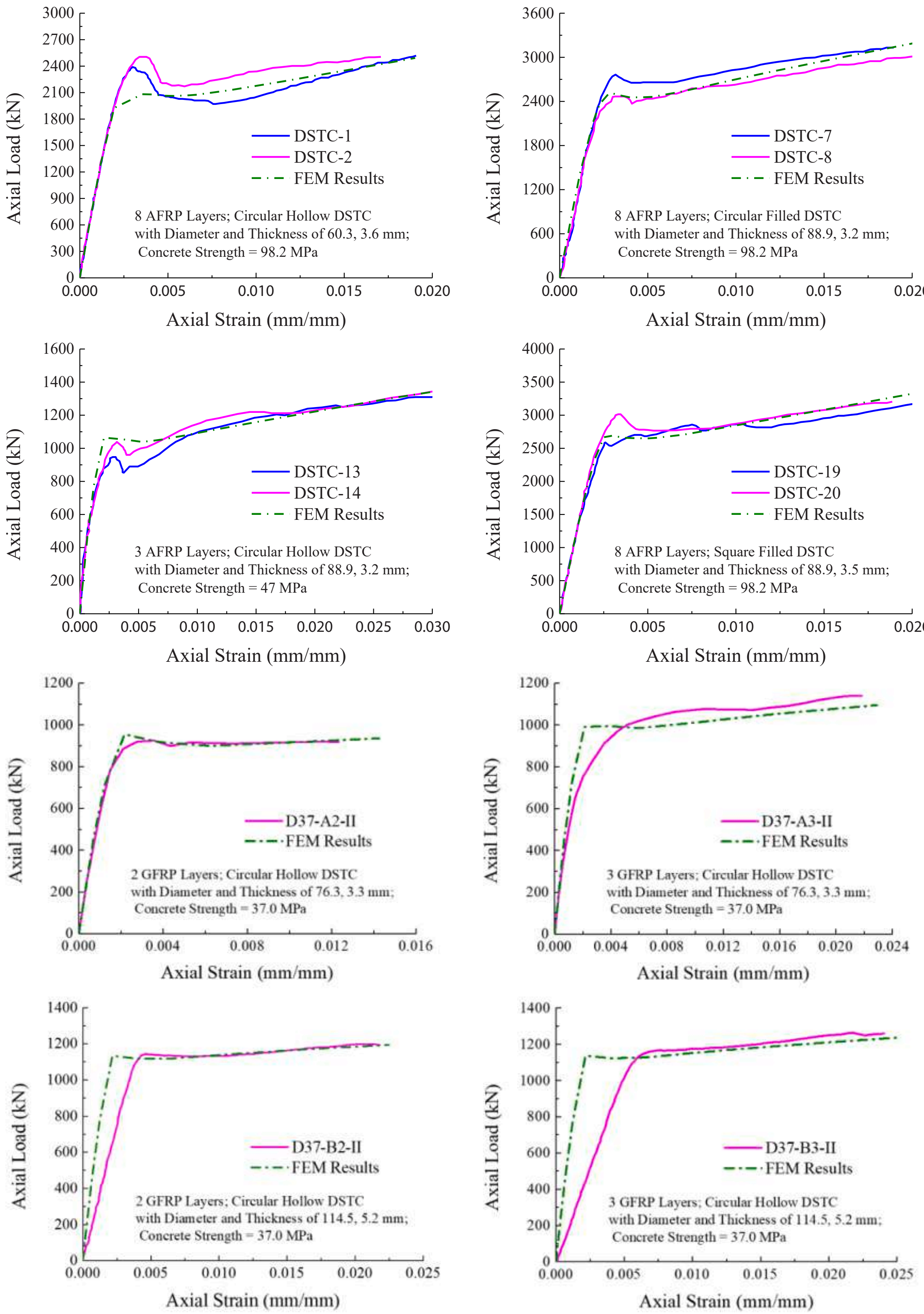

Fig. 5. (*continued*).

specimens exhibited about 38 % higher strain compared to circular inner tubes, indicating a pronounced ductility. Yet, this difference in ductility was not prominently observed in filled DSTC specimens.

The response of Group G4 specimens was analogous to that of Group G1 concerning ultimate axial load capacity, albeit with a marginally lower increase percentage. However, the behavior in ultimate axial strain did not exhibit a clear pattern favoring a particular steel tube shape. The observed behavior was influenced by another variable, the concrete compressive strength. For higher compressive strength values, hollow tubes with square cross-sections displayed better ductility compared to circular ones, a trend which reversed in the case of filled tubes. As the compressive strength diminished, the behavior inverted,

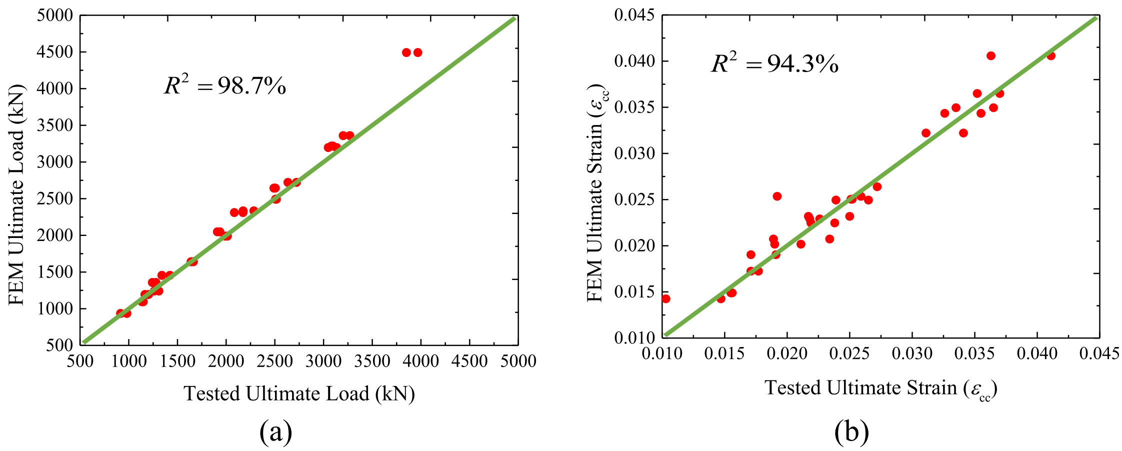

Fig. 6. Correlation between Experimental and Finite Element Predictions for: ultimate Axial Load. (b) Ultimate Axial Strain.

indicating the superiority of circular tubes over square for hollow tubes and vice versa for filled tubes.

Lastly, the performance of specimen groups G5 and G6 mirrored the characteristics observed in groups G2 and G3, further substantiating the observed trends. Comprehensive details regarding the influence of inner tube shape on ultimate axial strength and ultimate strain are documented and visually represented in Fig. 9, providing a deeper understanding of the structural behavior under varied conditions.

4.6.5. Effect of steel tube arrangement (i.e., Single, Double)

The configuration of steel tubes was found to markedly influence the ultimate axial load capacity of DSTC specimens. The data indicated that the incorporation of dual steel tubes resulted in a notable enhancement of axial strength, ranging from 22.3 % to 45.6 %. This augmentation can be primarily attributed to the superior material properties of steel relative to concrete in scenarios involving a single tube. Correspondingly, there was a significant elevation in ultimate strain, with an increase of approximately 51.8–118.3 %. This suggests an improved ductility in specimens featuring double steel tubes as opposed to their single-tube counterparts. For a comprehensive analysis and graphical representation of these findings, refer to Fig. 10.

4.6.6. Effect of steel tube thickness & diameter

In the context of steel tube thickness and diameter, the behavior of hollow and filled DSTC sections, as observed in Group G1 specimens, presents intriguing dynamics. For hollow DSTC sections, an increase in the diameter and thickness of the steel tube was associated with a decrease in the ultimate axial load capacity. This phenomenon is likely a consequence of the diminished effective cross-sectional area, which in turn reduces the axial load-bearing capability. Conversely, in filled DSTC sections, an increase in the diameter and thickness of the steel tube correlates with an increase in ultimate axial load capacity, with an observed increase of approximately 30 %. This enhancement is attributable to the superior material strength of steel compared to concrete; as the proportion of steel in the cross section increases, so too does the load capacity.

When examining strain behavior, it was observed that for hollow DSTC sections, an increase in the size and thickness of the steel tube correlates with an increase in ultimate axial strain, suggesting enhanced ductility. This improvement in ductility can be attributed to the presence of steel, which bolsters the section's ductility as its proportion within the section escalates. However, for filled DSTC sections, the behavior of ultimate strain did not follow a definitive trend, exhibiting minor increases in some instances and decreases in others.

Groups G2 and G4 specimens mirrored the trends observed in Group G1, with filled DSTC specimens experiencing notable strength enhancements, reaching 80 % for G2 specimens and 61 % for G4 specimens. Concerning ultimate strain in filled DSTC specimens, an increase in the size and thickness of the steel tube led to improved ductility, a trend consistent with the higher steel ratios in the cross-section enhancing ductility.

Group G3 specimen results revealed that employing double steel tubes results in an approximate 26 % increase in ultimate axial strength as the size and thickness of the steel tubes are augmented. However, this trend was not mirrored in the ultimate strain, where no consistent behavior was observed. A similar pattern was noted in Group G6 specimens, with an observed increase in ultimate axial load capacity of around 37 %, while the ultimate strain did not display any definitive trend.

For a more detailed analysis of the impact of steel tube size and thickness on DSTC specimens, refer to Fig. 11.

Fig. 12 shows the FEM result for G2 and G3 specimens illustrating failure modes for columns with varying parameters. Group G3 specimen results revealed that employing double steel tubes results in an increase in ultimate axial strength as the size and thickness of the steel tubes are augmented. Group G2 specimens presented a distinct behavior pattern, particularly at lower concrete compressive strength values. Irrespective of the tubes being filled or hollow, DSTC specimens with square inner tubes consistently showed superior axial load resistance compared to those with circular inner tubes. Group G3 specimen results revealed that employing double steel tubes results in increase in ultimate axial strength as the size and thickness of the steel tubes are augmented. As can be seen in the figure, square hollow DSTC and circular hollow DSTC, ultimate axial load and strain is significantly higher.

5. Machine learning model development

5.1. Overview of the machine learning approach

ML has emerged as a transformative tool in structural engineering, enabling accurate predictions of complex phenomena that are challenging to model using conventional analytical or numerical methods. In this study, the objective of the ML model is to predict two critical parameters of FRP-confined columns subjected to monotonic compressive loading: the load-carrying capacity (P_{cu}) and the ultimate strain capacity (ε_{cc}). These parameters are functions of six key input features, as shown in Table 6, encompassing material properties and geometric characteristics, including the area of the concrete section, concrete strength, thickness of FRP wraps, elastic modulus of FRP, area of steel tubes, and the yield strength of steel tubes. The overarching goal is to build a robust predictive framework that can accurately model the non-linear relationships between these input variables and the output parameters,

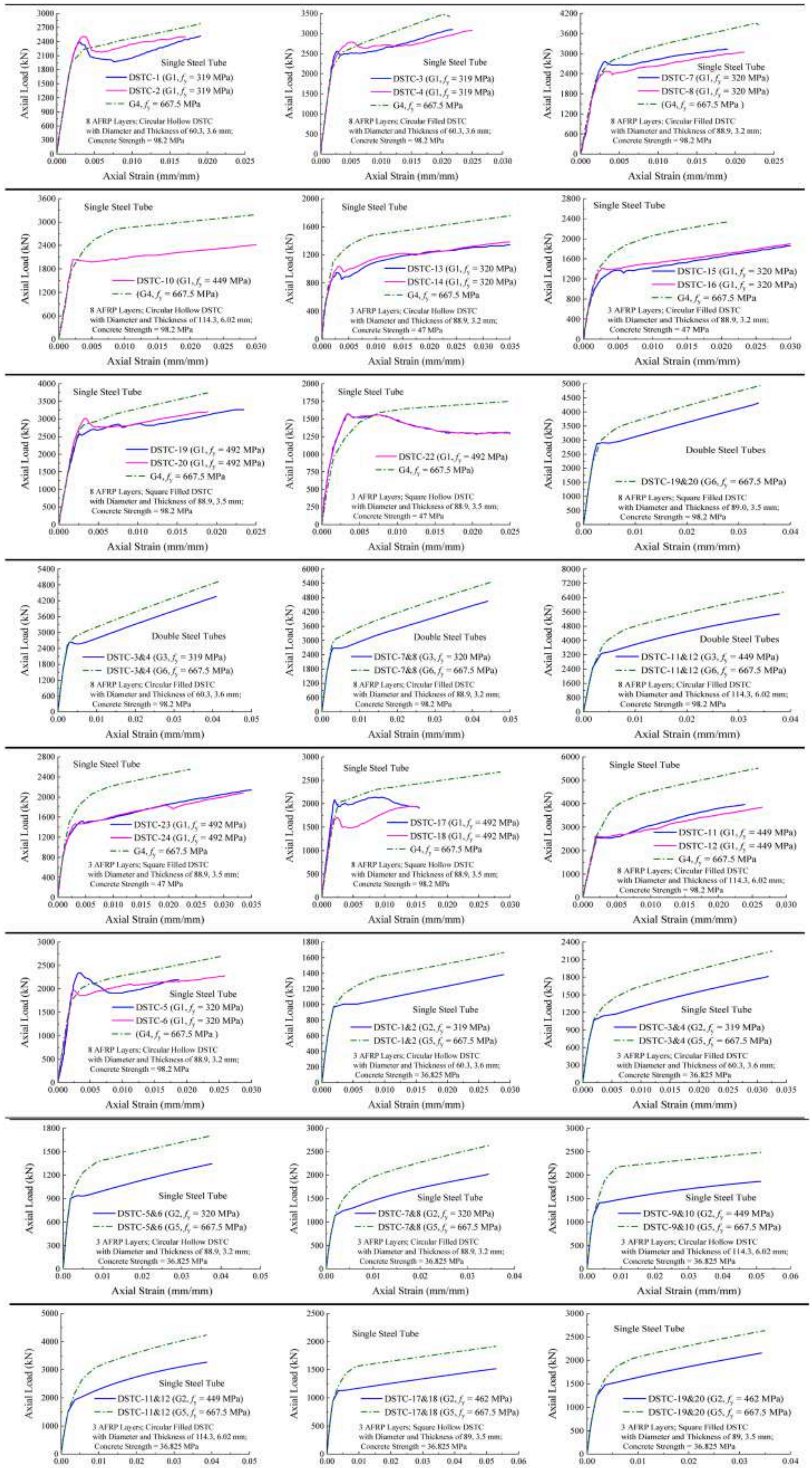

Fig. 7. Comparative load-strain curves for single and double steel tubed column specimens with varied yield strengths.

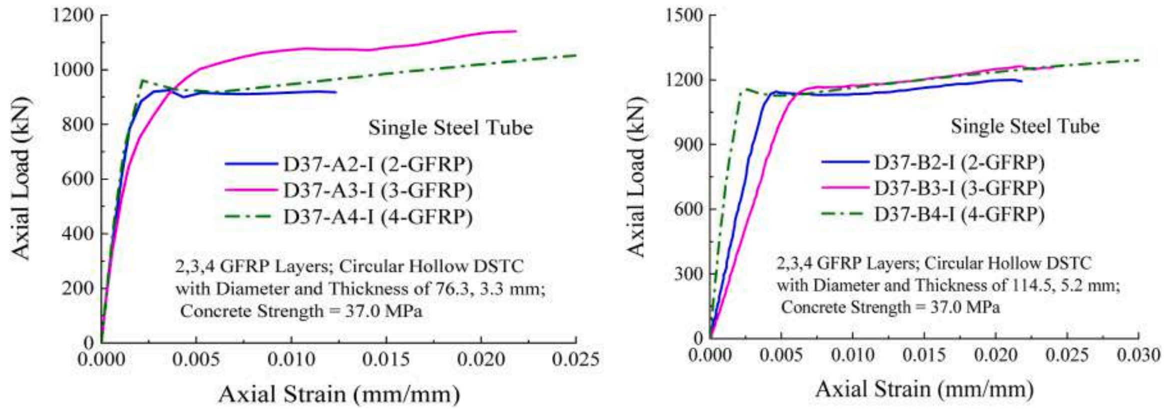

Fig. 8. Comparative analysis of ultimate axial load and strain enhancements in DSTC configurations with varying gfrp layer counts.

while also providing interpretable insights into the role of each feature.

A Deep Neural Network (DNN) was chosen as the predictive model due to its exceptional capacity to model high-dimensional, non-linear relationships in data. Compared to traditional regression models or simpler ML algorithms such as decision trees or support vector machines, DNNs offer a multilayered architecture capable of learning intricate patterns and interactions in the input space. This advantage is particularly relevant in the context of FRP-confined columns, where the interplay between material and geometric properties significantly influences structural performance. Existing literature underscores the suitability of DNNs for similar engineering applications.

The DNN architecture employed in this study consists of an input layer corresponding to the six input features, multiple hidden layers for feature transformation, and an output layer predicting the two target variables (P_{cu} and ε_{cc}). The hidden layers utilize rectified linear unit (ReLU) activation functions, which are well-suited for preventing vanishing gradient issues in deep networks given by Eq. (1). The Adam optimizer, an adaptive gradient-based optimization algorithm, was used to minimize the mean squared error (MSE) loss function, ensuring efficient convergence during training. To mitigate overfitting, dropout layers were incorporated into the architecture, randomly deactivating a fraction of neurons during training.

$$\mathrm{ReLU}(\boldsymbol{x}) = \mathbf{max}(\boldsymbol{0}, \boldsymbol{x}) \tag{1}$$

The selection of a DNN is further justified by its ability to generalize across diverse datasets, making it ideal for this study where the dataset exhibits high variability in material properties and geometric configurations. Moreover, the scalability of DNNs allows for future integration of additional input features, such as environmental conditions or load eccentricities, further broadening their applicability in structural engineering.

5.2. Dataset Analysis

5.2.1. Data Collection and Preparation

The dataset used in this study was assembled from experimental data and numerical simulations, incorporating a diverse range of configurations relevant to FRP-confined columns. The dataset consists of N = 116 samples, ensuring adequate representation of varying material and geometric properties critical to structural behavior.

Preprocessing was performed to prepare the dataset for input into the machine learning model. Feature scaling was applied to standardize the varying ranges of the input features. Since A_c (measured in mm^2) and E_f (measured in *MPa*) operate on different scales, min-max scaling was used to transform all features to a range of [0,1] by using Eq. (2). This transformation ensures uniform contribution to the training of the machine learning model and avoids bias introduced by features with larger magnitudes.

$$\boldsymbol{x}' = \frac{\boldsymbol{x} - \boldsymbol{x}_{\min}}{\boldsymbol{x}_{\max} - \boldsymbol{x}_{\min}} \tag{2}$$

Where, $x_{\min}$ is the minimum of the feature, and $x_{\max}$ is the maximum value of the feature.

This scaling approach ensures uniform contribution of each feature to the machine learning model, preventing bias introduced by large magnitudes. Fig. 13 displays box plots of the input features before scaling, revealing significant disparities in their distributions and the presence of outliers. Feature Ef and As was found having outliers presence as seen in Figs. 13 and 14.

In addition to scaling, normalization was applied to address skewness in feature distributions. Outputs such as ε_{cc} exhibited pronounced skewness, which was mitigated using log transformations. This step is crucial for stabilizing variance and enhancing the model's learning capabilities. Post-normalization, the scaled features exhibited uniform distributions, as illustrated in Fig. 14, further supporting effective model training.

To ensure robust model development, the dataset was split into training, validation, and testing subsets using a 70–15–15 ratio. Stratified sampling was employed to maintain balanced representation of critical features such as t_f and E_f, which showed significant variability across samples. This stratification was essential for exposing the model to a comprehensive range of feature combinations during training and validation, ultimately improving its generalization capabilities.

5.2.2. Exploratory Data Analysis (EDA)

The dataset comprises eight key variables, including input features (A_c, f_c', t_f, E_f, A_s, f_y) and output variables (P_{cu}, ε_{cc}), as described in Table 7. The mean, standard deviation, minimum, maximum, variance, skewness, and kurtosis of each variable were computed to understand their statistical properties.

From the table, A_c exhibits a mean of 18,294.75 mm^2 with a standard deviation of 3634.6, indicating moderate variability. The skewness of −0.66 and kurtosis of −1.00 suggest that the distribution is slightly negatively skewed with thinner tails. f_c' shows a higher variability (std. dev = 29.6 MPa) and is almost symmetrically distributed (Skewness=0.13), reflecting a balanced representation of low and high-strength concrete samples. t_f and E_f have notably smaller ranges, with t_f showing a minimal skewness of 0.13 and E_f a pronounced negative skewness of −1.93, indicative of a bias towards higher elastic modulus values.

A_s and *fy* exhibit moderate variability, with *fy* having a slightly negatively skewed distribution (-0.46), while P_{cu}, the load-carrying capacity, demonstrates the highest variability (std. dev = 1159.35 kN) and a significant positive skewness (1.13), indicating a concentration of lower values and a few high outliers. Similarly, ε_{cc} has a relatively small

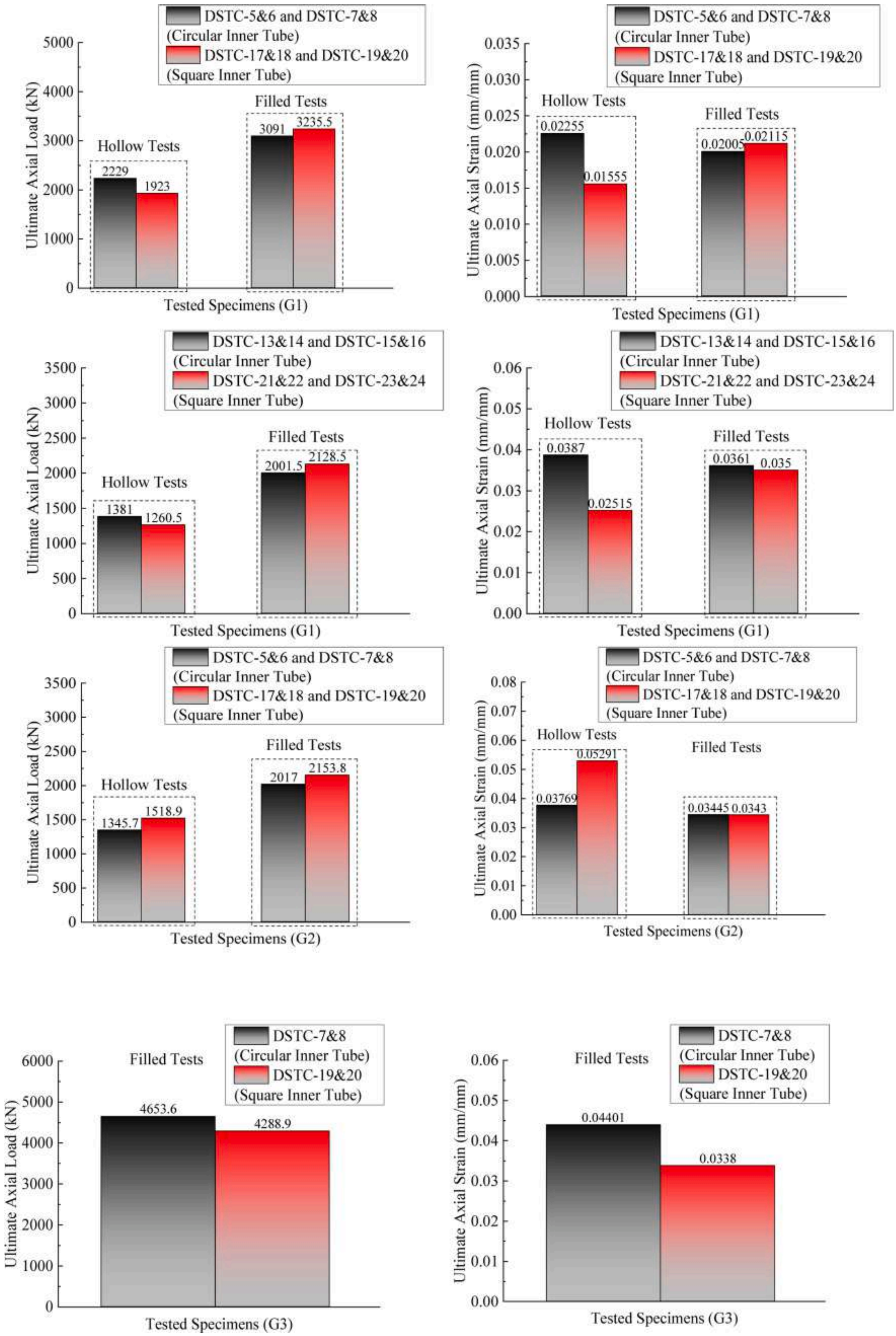

Fig. 9. Comparative analysis of ultimate axial strength and strain in DSTC specimens: assessing the influence of inner tube geometry across different specimen groups.

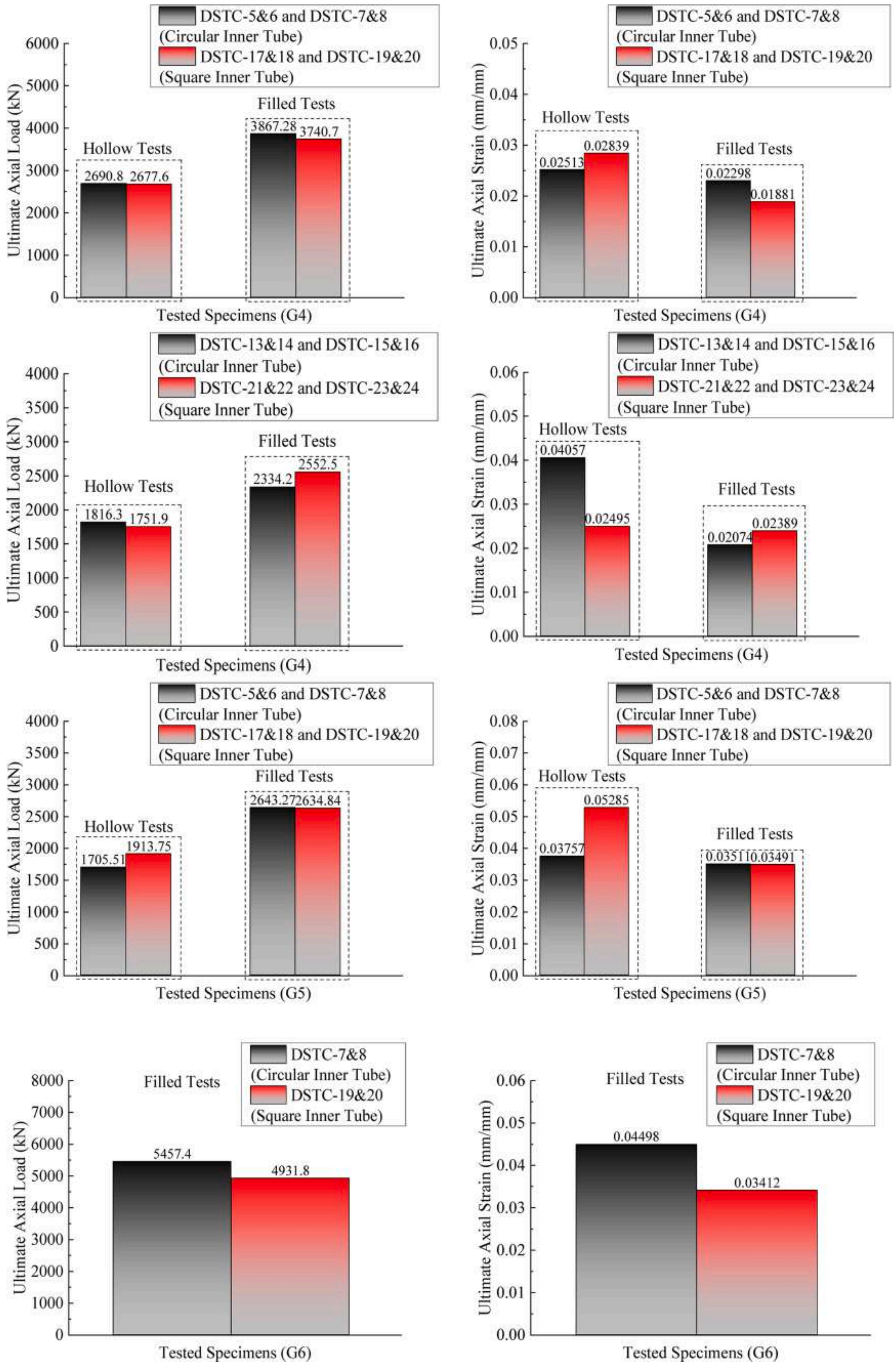

Fig. 9. (*continued*).

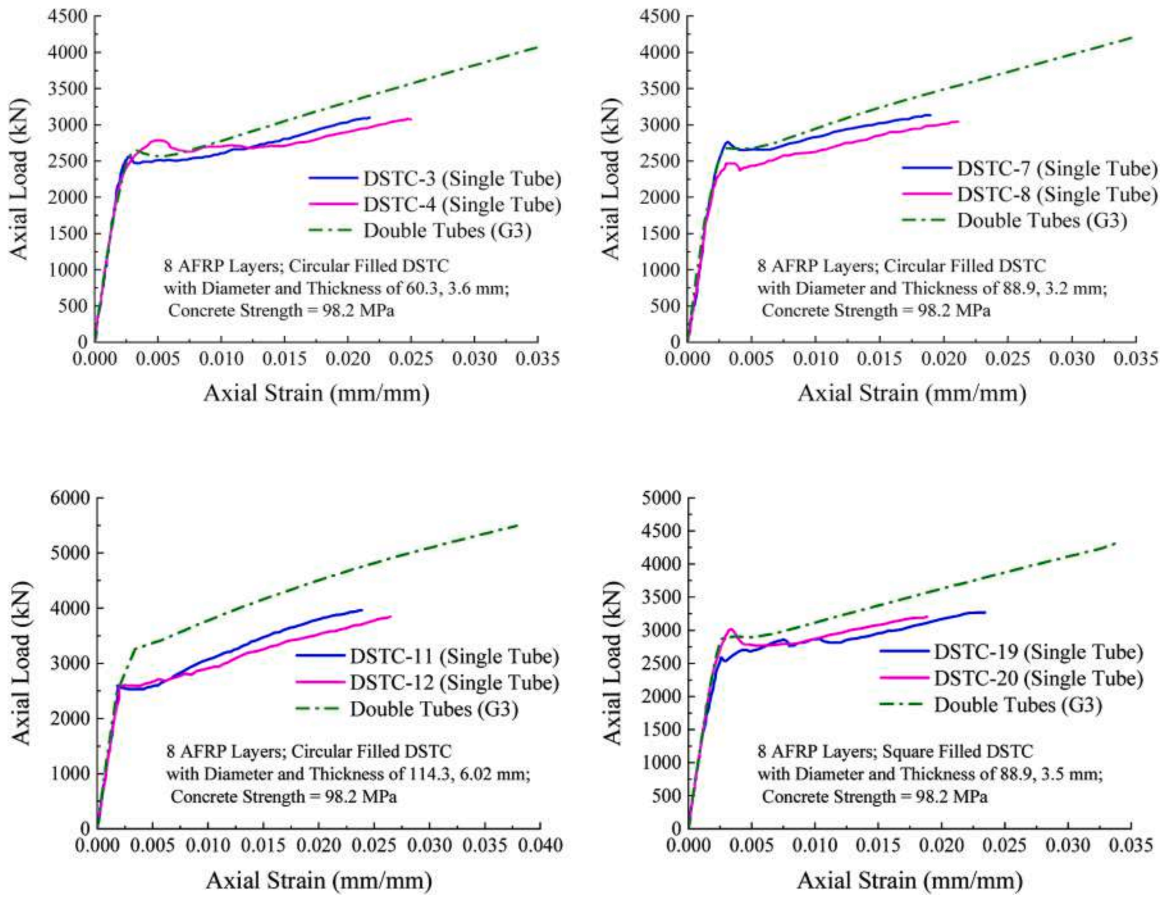

Fig. 10. Comparative analysis of axial load capacity and ultimate strain in DSTC specimens: single vs. double steel tube configurations.

range (mean = 0.03 mm/mm), with a near-symmetric distribution (Skewness=0.58).

Fig. 15 provides a visual representation of these statistics. The top plots highlight the mean and standard deviation of variables, showing E_f as the most significant contributor to variability. The variance plot underscores the dominance of E_f and A_c in the dataset, while the skewness and kurtosis plot confirm the near-normal distribution of most variables with some exceptions like E_f and P_{cu}.

The histogram distributions with kernel density estimation (KDE), shown in Fig. 16, provide deeper insights into the data distributions. For A_c, the distribution is unimodal and slightly left-skewed. $f_c^{'}$ and t_f demonstrate bimodal distributions, due to the grouping of data into distinct concrete strengths and FRP configurations. E_f, on the other hand, shows a highly concentrated distribution near its maximum values, reflecting the dominance of high-stiffness materials in the dataset. Similarly, A_s and f_y have distributions skewed towards lower values, with f_y showing a larger concentration below 500 MPa. The output P_{cu} is positively skewed, as reflected in the heavy tail of the distribution, and ε_{cc} is almost uniform with a slight peak around its mean value.

The relationships between variables were explored using both Pearson and Spearman correlation coefficients, depicted in Figs. 17 and 18, respectively. Pearson correlation measures linear relationships, while Spearman ranks the correlations, making it more robust to non-linear trends.

Fig. 17, the Pearson correlation heatmap, reveals strong positive correlations between t_f and $f_c^{'}$ (0.98) and between P_{cu} and t_f (0.70), indicating the significant role of FRP thickness in determining load-carrying capacity. Moderate correlations are also observed between E_f and A_c (0.47), and between P_{cu} and $f_c^{'}$ (0.66), suggesting the combined influence of elastic modulus and concrete strength on structural performance. Interestingly, A_s exhibits a negative correlation with A_c (-0.49), due to design trade-offs in column dimensions.

Fig. 18, the Spearman correlation heatmap, highlights similar trends but with stronger correlations in some cases. For instance, t_f shows an even stronger rank correlation with P_{cu} (0.81), underscoring its critical impact. A_s has a positive correlation with ε_{cc} (0.31), suggesting a potential relationship between steel area and strain capacity under compression.

5.3. Methodology

5.3.1. Model architecture

The DNN architecture developed in this study is designed to effectively model the complex, non-linear relationships between the input features and the target variables P_{cu} and ε_{cc} The architecture consists of

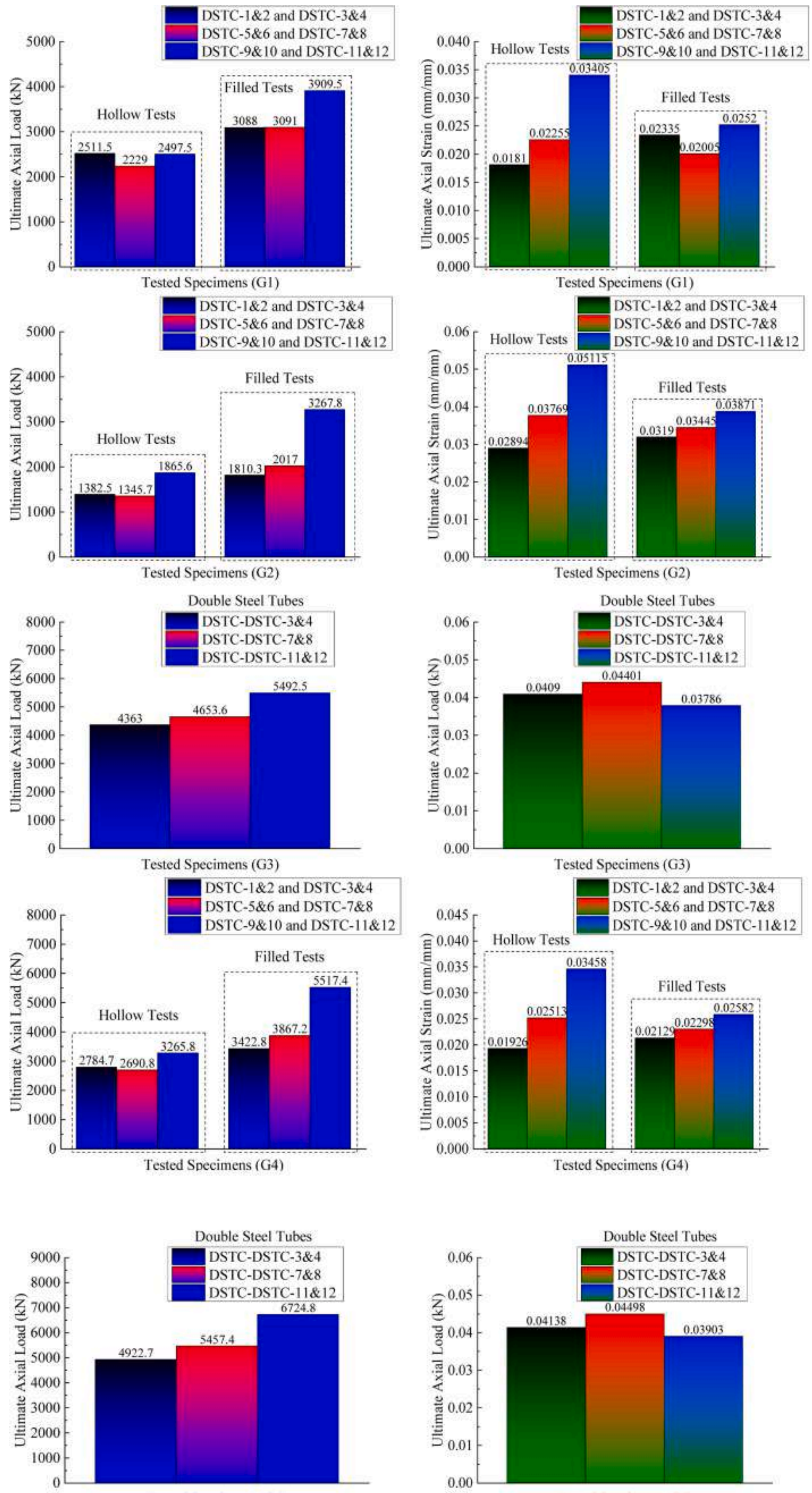

Fig. 11. Influence of steel tube diameter and thickness on ultimate axial load capacity and strain in hollow and filled DSTC specimens.

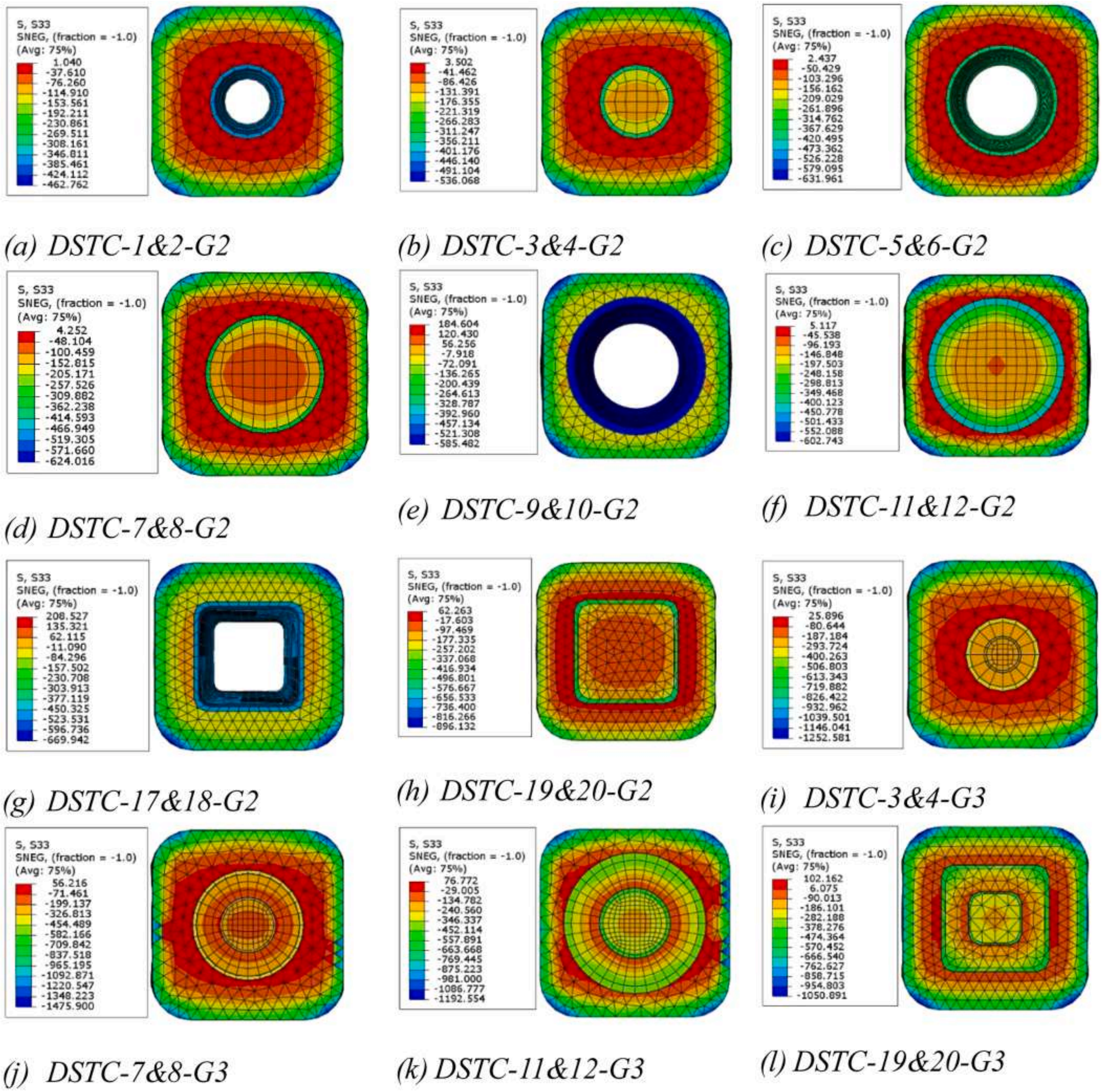

Fig. 12. Failure modes for columns with varying parameters.

Table 6
Variables with their unit and description.

Variable	Unit	Description
A_c	mm^2	Area of concrete section
f_c	MPa	Concrete strength of unconfined concrete
t_f	mm	Total thickness of FRP wraps
E_f	MPa	Elastic modulus of FRP
A_s	mm^2	Area of steel tubes
f_y	MPa	Yield strength of internal steel tubes
P_{cu}	kN	Load carrying capacity of the FRP-confined column
ε_{cc}	mm/mm	Ultimate strain capacity of FRP-confined column

an input layer, multiple hidden layers, and an output layer, as depicted in Fig. 19.

The input layer comprises six neurons, each corresponding to one of the standardized input features detailed in Table 6. These features were selected based on their significant impact on the compressive behavior of FRP-confined columns.

The network includes three hidden layers, each containing 64 neurons. This configuration was determined through hyperparameter tuning to balance model complexity and computational efficiency. The hidden layers employ the ReLU activation function, which is given by Eq. (1).

The ReLU function introduces non-linearity into the model, allowing it to learn complex patterns within the data while mitigating the vanishing gradient problem commonly encountered in deep networks. To prevent overfitting and enhance the generalization capability of the

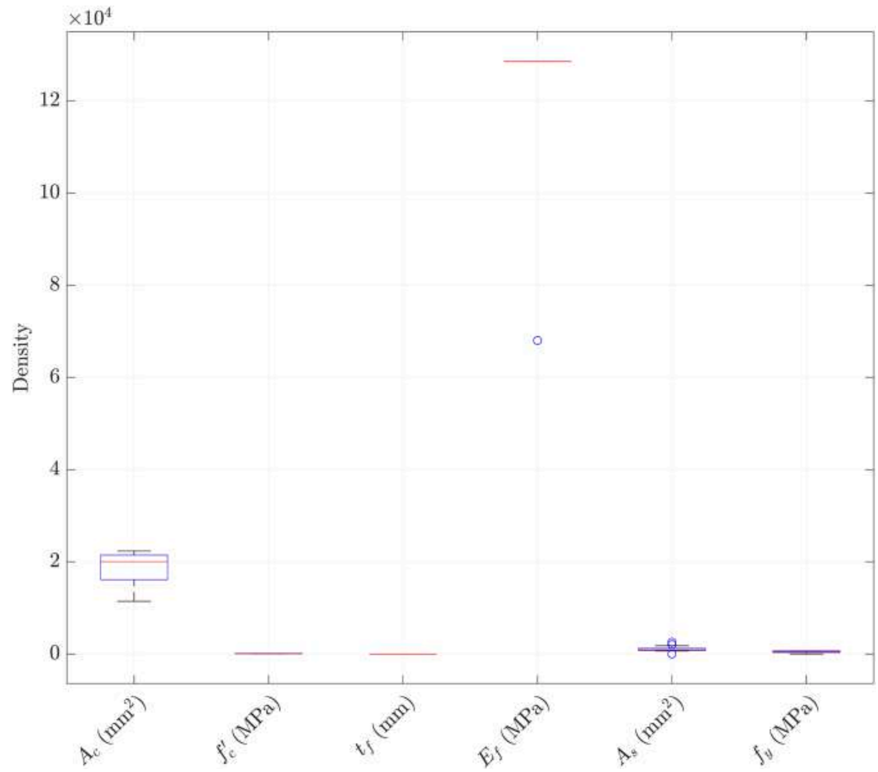

Fig. 13. Box plot of input features with outliers.

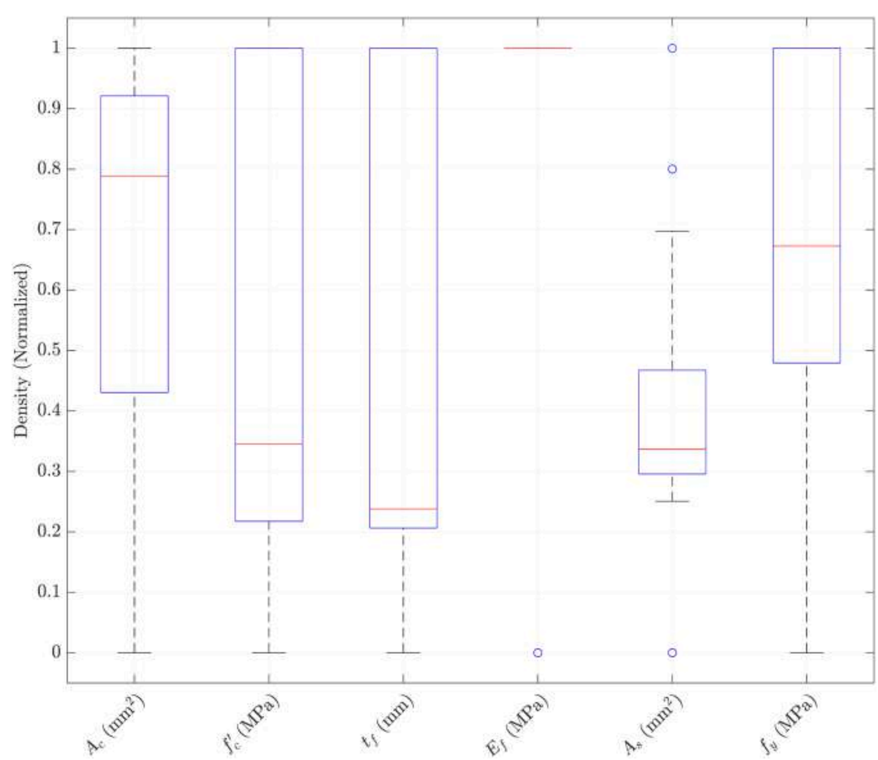

Fig. 14. Box plot of scaled input features with outliers.

Table 7
Statistical descriptive analysis of the dataset.

Variable	Mean	Std. Dev	Min	Median	Max	Variance	Skewness	Kurtosis	Q1	Q3	(Q3 - Q1)
A_c	18294.75	3634.60	11427.66	20027.83	22332.57	13210300.00	−0.66	−1.00	16122.91	21470.67	5347.77
f_c	65.94	29.60	20.00	47.00	98.20	876.11	0.13	−1.90	37.00	98.20	61.20
t_f	1.03	0.52	0.34	0.64	1.60	0.27	0.13	−1.91	0.60	1.60	1.00
E_f	119112.07	22000.21	68000.00	128500.00	128500.00	484009000.00	−1.93	1.75	128500.00	128500.00	0.00
A_s	1109.03	575.58	0.00	861.90	2560.82	331297.34	0.38	−0.11	757.11	1197.00	439.89
f_y	431.42	177.42	0.00	449.00	667.50	31477.00	−0.46	0.39	320.00	667.50	347.50
P_{cu}	2451.62	1159.35	916.00	2263.79	6724.78	1344092.83	1.13	1.27	1579.48	3115.00	1535.52
ε_{cc}	0.03	0.01	0.01	0.03	0.05	0.00	0.58	−0.07	0.02	0.03	0.01

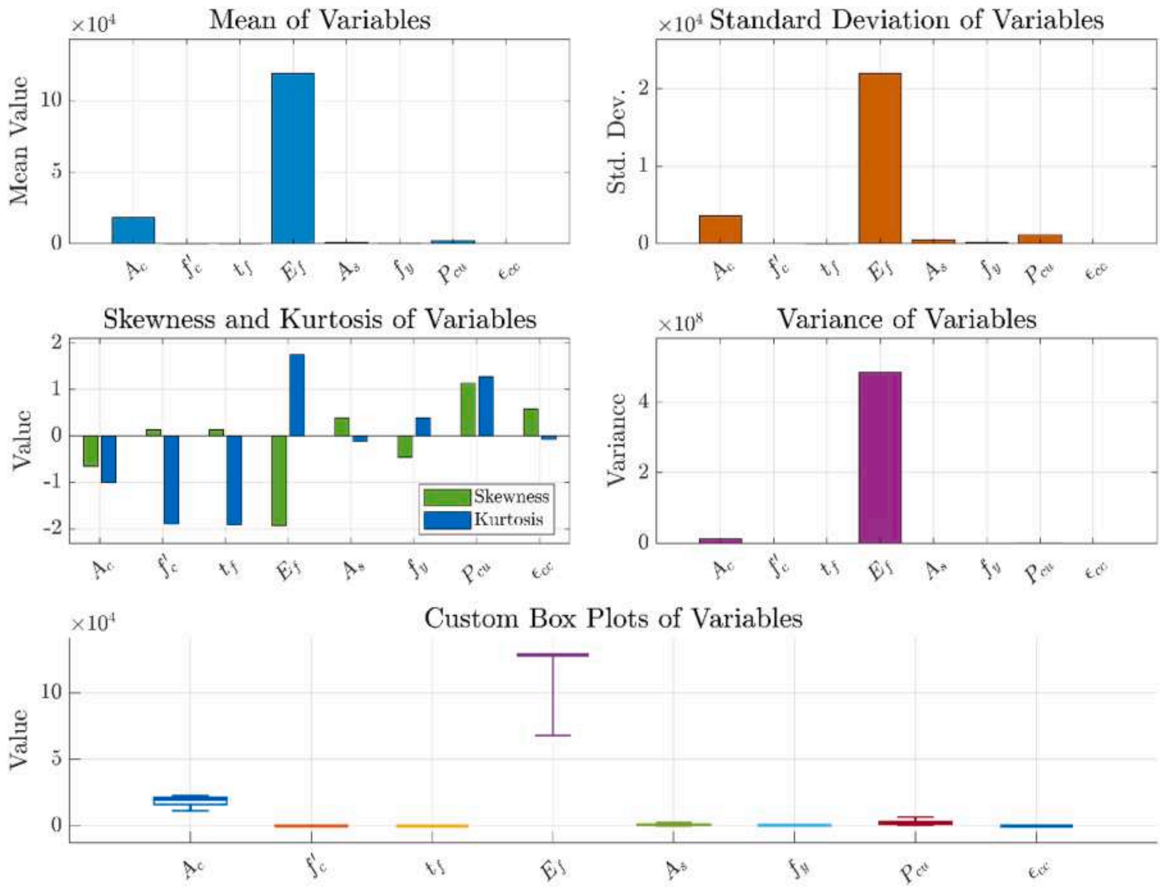

Fig. 15. Various statistical analysis of the variables in the dataset.

model, dropout regularization layers with a dropout rate of 20 % were inserted after each hidden layer. This technique randomly deactivates a fraction of neurons during training, forcing the network to learn more robust features.

The output layer consists of two neurons corresponding to the target variables: P_{cu} and ε_{cc} of the FRP-confined columns. Since these are continuous variables, no activation function was applied to the output layer, allowing the network to output a wide range of real values.

Key hyperparameters were carefully selected to optimize the performance of the DNN. Table 8 summarizes the hyperparameters used in the model.

The Adam optimizer was chosen for its efficiency and adaptive learning rate capabilities, which are beneficial for training deep networks. A learning rate of 0.001 was set to ensure stable convergence. The batch size was fixed at 32, a common choice that provides a good balance between training speed and model stability.

The DNN was implemented using the TensorFlow and Keras libraries, which offer high-level APIs for constructing and training deep learning models. The model's architecture is outlined in Algorithm 1.

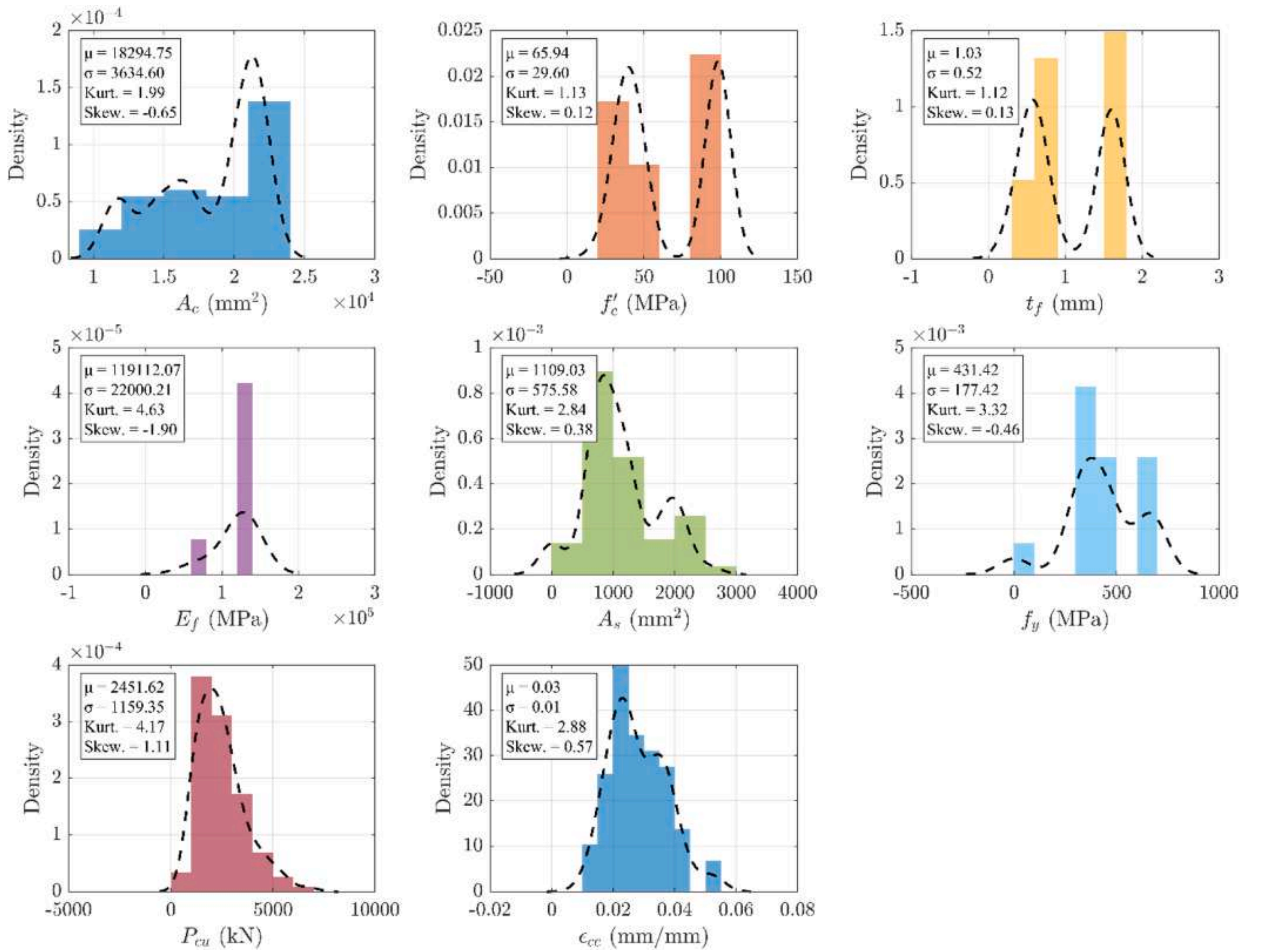

Fig. 16. Histogram distribution plot with KDE of variables.

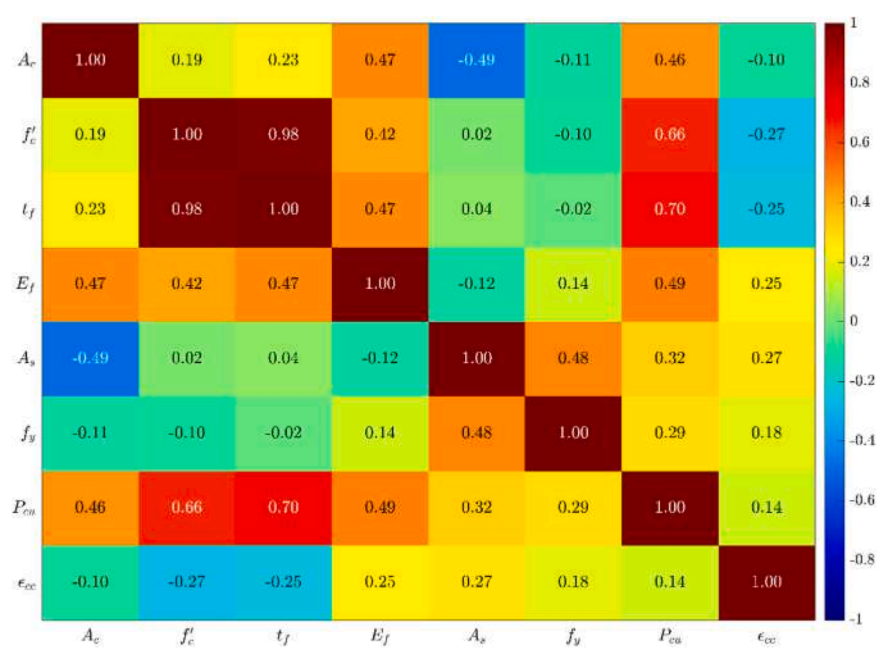

Fig. 17. Pearson correlation heatmap with correlation value.

Fig. 18. Spearman correlation rank correlation heatmap.

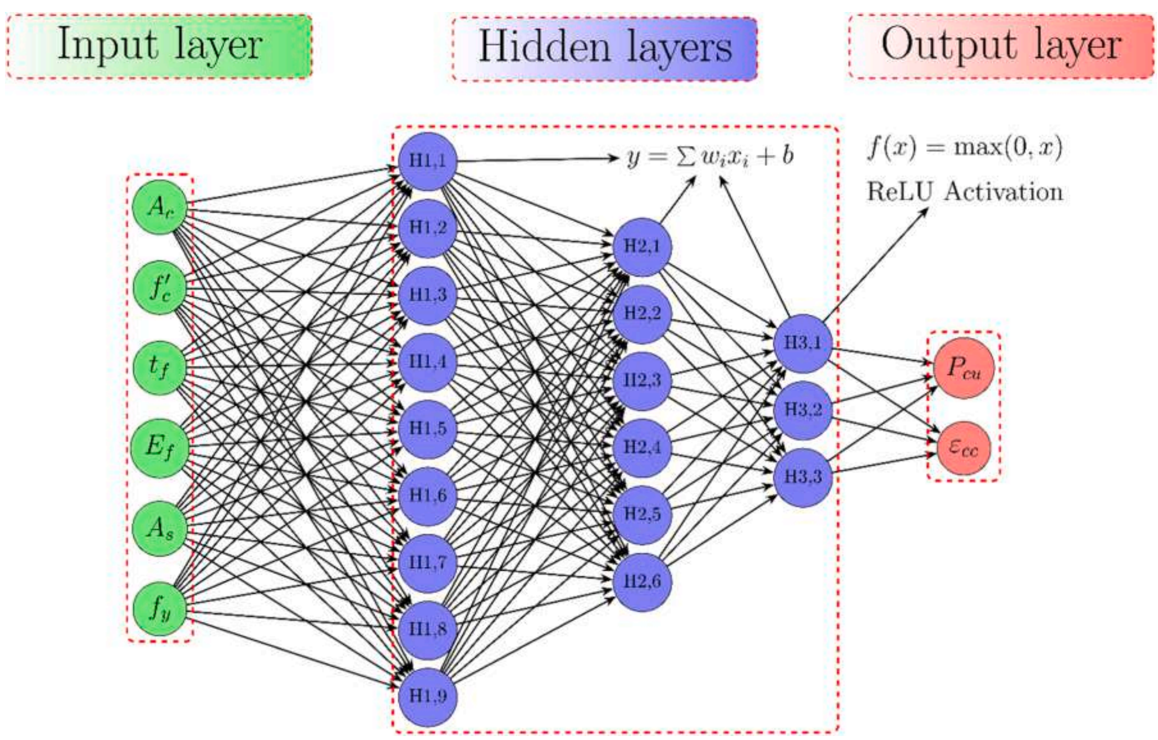

Fig. 19. DNN model architecture with input, hidden and output layers.

Table 8
Hyperparameters of the DNN Model.

Hyperparameter	Value
Number of hidden layers	3
Neurons per hidden layer	64
Activation function	ReLU
Dropout rate	20 %
Optimizer	Adam
Learning rate	0.001
Batch size	32
Number of epochs	100
Loss function	Mean Squared Error

Algorithm 1. pseudocode of the DNN Architecture

```
Initialize a sequential model
Add an input layer with 6 neurons
Add a hidden layer with 64 neurons and ReLU activation
Apply a dropout layer with a rate of 0.2
Add a second hidden layer with 64 neurons and ReLU activation
Apply a dropout layer with a rate of 0.2
Add a third hidden layer with 64 neurons and ReLU activation
Apply a dropout layer with a rate of 0.2
Add an output layer with 2 neurons
Compile the model using the Adam optimizer and MSE loss function
```

5.3.2. Training process

The model was trained using the preprocessed dataset, with the data split into training (70 %), validation (15 %), and testing (15 %) sets to evaluate the model's performance on unseen data. Stratified sampling ensured that each subset adequately represented the variability in the dataset, particularly for features with significant skewness or outliers.

During training, the MSE loss function was minimized using the Adam optimizer. Early stopping was implemented to halt training when the validation loss ceased to improve for a consecutive number of epochs, thus preventing overfitting.

5.3.3. Model validation

The performance and reliability of the developed DNN model were rigorously evaluated using several statistical metrics and a robust validation strategy. This section details the metrics used for performance evaluation and the cross-validation and hyperparameter tuning approach adopted, leveraging Bayesian optimization techniques.

To assess the predictive accuracy of the DNN model, four key performance metrics were employed: the coefficient of determination (R^2), RMSE, Mean Absolute Error (MAE), and Mean Absolute Percentage Error (MAPE). These metrics provide comprehensive insights into the model's ability to generalize and accurately predict the target variables P_{cu} and ε_{cc}

The R^2 metric quantifies the proportion of variance in the dependent variable that is predictable from the independent variables. It is defined using Eq. (3):

$$\boldsymbol{R}^2 = \mathbf{1} - \frac{\sum_{i=1}^{n}(\boldsymbol{y}_i - \widehat{\boldsymbol{y}}_i)^2}{\sum_{i=1}^{n}(\boldsymbol{y}_i - \overline{\boldsymbol{y}})^2} \tag{3}$$

where:

- y_i is the actual value,
- $\widehat{y}_i$ is the predicted value,
- $\overline{y}$ is the mean of the actual values,
- n is the number of observations.

An R^2 value closer to 1 indicates a better fit of the model to the data.

RMSE measures the average magnitude of the prediction errors, providing a quadratic scoring rule that penalizes large errors more severely. It is calculated using Eq. (4).

$$\text{RMSE} = \sqrt{\frac{\mathbf{1}}{\boldsymbol{n}}\sum_{i=1}^{n}(\boldsymbol{y}_i - \widehat{\boldsymbol{y}}_i)^2} \tag{4}$$

Lower RMSE values indicate better model performance.

MAE provides the average absolute difference between predicted and actual values, offering a linear score that equally weights all differences. It is given by Eq. (5).

$$\text{MAE} = \frac{\mathbf{1}}{\boldsymbol{n}}\sum_{i=1}^{n}|\boldsymbol{y}_i - \widehat{\boldsymbol{y}}_i| \tag{5}$$

MAPE expresses the prediction error as a percentage, providing a normalized measure of the predictive accuracy, given by Eq. (6).

$$\text{MAPE} = \frac{\mathbf{100\backslash\%}}{\boldsymbol{n}}\sum_{i=1}^{n}\left|\frac{\boldsymbol{y}_i - \widehat{\boldsymbol{y}}_i}{\boldsymbol{y}_i}\right| \tag{6}$$

This metric is particularly useful for comparing errors across datasets with different scales.

The robustness and generalization capability of the DNN model heavily depend on the appropriate selection of hyperparameters. To optimize these parameters and prevent overfitting, a cross-validation strategy coupled with Bayesian optimization was employed.

Furthermore, k-fold cross-validation was utilized to assess the model's performance across different subsets of the data. The dataset was partitioned into $k = 5$ folds for balancing bias and variance. In each iteration, four folds were used for training, and one fold was reserved for validation. This process was repeated five times, ensuring that each fold served as the validation set once.

This approach provides a more reliable estimate of the model's performance on unseen data by reducing the variance associated with a single train-test split. It also helps in identifying any potential overfitting or underfitting issues.

In addition, Bayesian optimization was adopted for hyperparameter tuning due to its efficiency in handling expensive function evaluations and its ability to converge to optimal solutions with fewer iterations compared to grid or random search methods. Table 9 presents key hyperparameters selected for optimization with description and search boundaries.

Table 9
Key hyperparameters and their search space selection for optimization.

Hyperparameter	Description	Values Explored
Number of Hidden Layers (LLL)	Explored values between 2 and 10.	2, 3, 4, 5, 6, 7, 8, 9, 10
Neurons per Hidden Layer (NNN)	Ranged from 32 to 128 neurons.	32, 64, 96, 128
Learning Rate (η)	Considered values between 1e−5 and 1e−2.	0.00001, 0.0001, 0.001, 0.01
Batch Size (BBB)	Tested batch sizes of 16, 32, 64, and 128.	16, 32, 64, 128
Dropout Rate (DDD)	Varied between 0 % and 50 %.	0 %, 10 %, 20 %, 30 %, 40 %, 50 %

Table 10
Model Performance Metrics to predict outputs.

Metric	P_{cu} (LR)	ε_{cc} (LR)	P_{cu} (SVR)	ε_{cc} (SVR)	P_{cu} (RFR)	ε_{cc} (RFR)	P_{cu} (GBR)	ε_{cc} (GBR)	P_{cu} (DNN)	ε_{cc} (DNN)
R^2	0.9047	0.5511	0.7074	0.2566	0.9547	0.9027	0.9926	0.9389	0.9973	0.9646
RMSE	315.13	0.0081	552.16	0.0104	217.2	0.0038	87.85	0.003	85.25	0.0022
MAE	275.73	0.0066	328.5	0.0091	124.38	0.0025	71.27	0.0019	67.15	0.0013
MAPE (%)	13.69	29.43	15.24	41.11	5.2	9.65	3.61	7.48	3.2	6.92

Algorithm 2. outlines the Bayesian optimization process used for hyperparameter tuning.

Initialize the search space for hyperparameters $\Theta = \{L, N, \eta, B, D\}$.
Define the objective function $f(\Theta)$ as the validation loss obtained from cross-validation.
Initialize the Gaussian process surrogate model with initial observations.
while stopping criterion not met **do**
    Select next hyperparameter set Θ' by optimizing the acquisition function.
    Evaluate $f(\Theta')$ via cross-validation.
    Update the surrogate model with new observation $(\Theta', f(\Theta'))$.
end while
return the hyperparameters Θ^* that minimize $f(\Theta)$.

The acquisition function used was the Expected Improvement (EI), which balances exploration and exploitation by considering both the mean and uncertainty predictions of the surrogate model.

5.4. Model Interpretation with SHAP Analysis

Understanding the decision-making process of complex machine learning models, such as deep neural networks, is essential for validating their predictions and gaining insights into the underlying data relationships. Shapley Additive Explanations (SHAP) provide a unified framework for interpreting model predictions by assigning each feature an importance value based on cooperative game theory.

SHAP values quantify the contribution of each input feature to the prediction of a specific instance, allowing for a detailed analysis of feature importance. This approach considers all possible combinations of features, ensuring that the attribution of importance is fair and consistent. The SHAP value for a feature represents the average marginal contribution of that feature across all possible subsets of features given by Eq. (7).

$$\boldsymbol{\phi}_i = \sum\nolimits_{S\subseteq F\setminus\{i\}} \frac{|\boldsymbol{S}|!(|\boldsymbol{F}| - |\boldsymbol{S}| - \mathbf{1})!}{|\boldsymbol{F}|!}[\boldsymbol{v}(\boldsymbol{S}\cup\{\boldsymbol{i}\}) - \boldsymbol{v}(\boldsymbol{S})] \tag{7}$$

where:

- ϕ_i is the SHAP value for feature iii,
- F is the set of all features,
- S is a subset of features not containing feature iii,
- $v(S)$ is the model's prediction when only features in subset SSS are present.

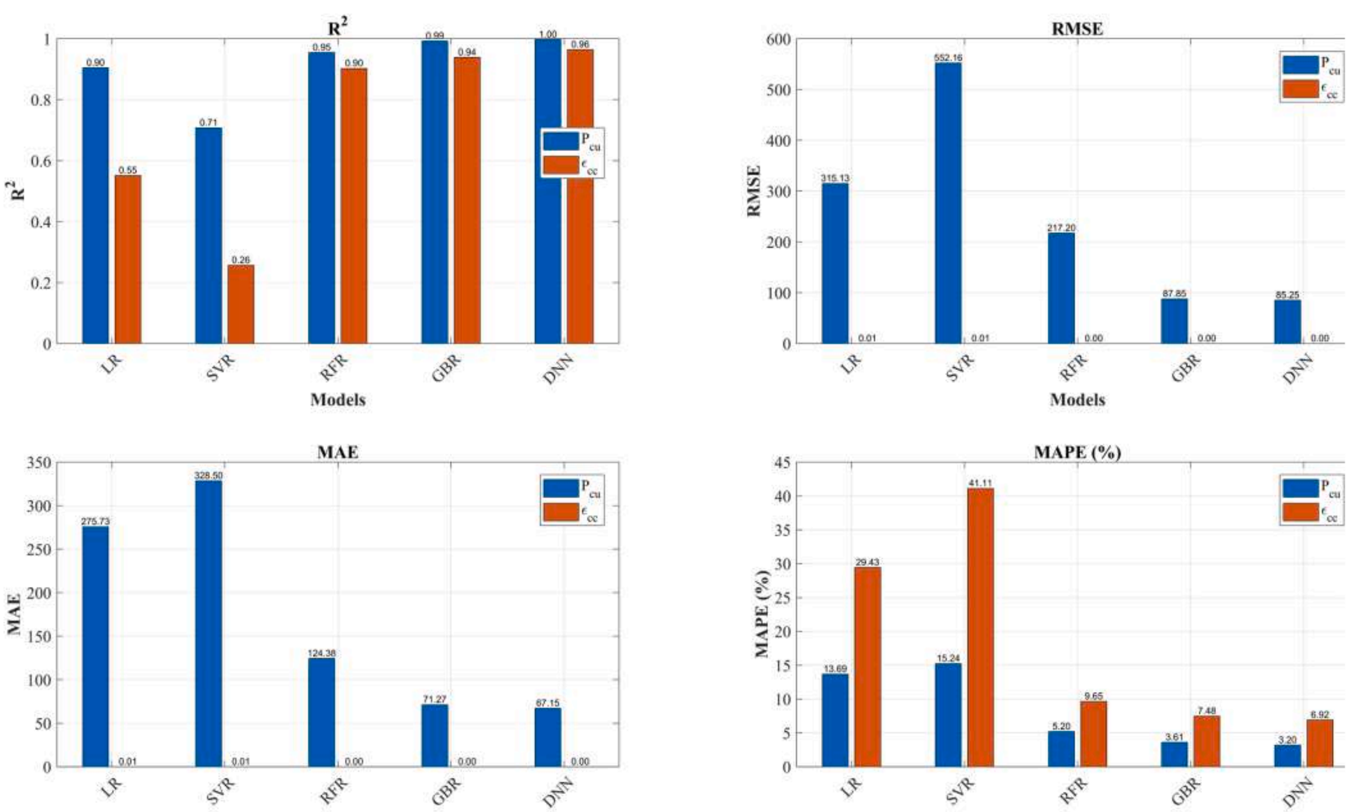

Fig. 20. Model performance metrics to predict P_{cu} and ε_{cc}.

In this equation, the term $\frac{|S|!(|F|-|S|-1)!}{|F|!}$ represents the weighting factor based on the number of features, ensuring that all subsets are equally considered. The difference $v(S \cup \{i\}) - v(S)$ captures the change in the prediction when feature iii is added to subset S, reflecting its marginal contribution.

Applying SHAP analysis to our DNN model enables us to interpret how each of the six input features influences the predicted P_{cu} and ultimate strain capacity ε_{cc}.

Each feature's SHAP value represents its contribution to pushing the model's output from the base value (the average prediction over the training data) towards the actual prediction for that instance. By aggregating SHAP values across all instances in the dataset, we can obtain a global interpretation of feature importance. This aggregated analysis highlights which features consistently have the most significant impact on the model's predictions, provides valuable insights into the factors that most influence the structural performance of FRP-confined columns.

Furthermore, SHAP values facilitate the detection of any anomalies or unexpected patterns in the model's behavior. If certain features exhibit inconsistent or counterintuitive SHAP values, it may prompt a re-examination of the data or model assumptions, ensuring the model's reliability and validity.

The advantages of using SHAP for model interpretation include:

- **Consistency**: SHAP values guarantee consistent feature attribution, ensuring that features contributing more to the model's predictions receive higher importance scores.
- **Local and Global Interpretability**: SHAP provides both instance-level (local) explanations and overall (global) feature importance, offering a comprehensive understanding of the model.
- **Model-Agnostic**: SHAP can be applied to any machine learning model, including complex ones such as DNNs, without requiring modifications to the model structure.

5.5. Results and discussion

5.5.1. Model performance

The predictive performance of different machine learning models was evaluated on the basis of P_{cu} and ε_{cc}. Key metrics including R^2, RMSE, MAE, and MAPE were used to quantitatively assess the models. The results for all models, including LR, SVR, RFR, GBR, and DNN, are summarized in Table 1.

The R^2 values for P_{cu} indicate that DNN achieved the best performance ($R^2 = 0.9973$), followed closely by GBR ($R^2 = 0.9926$). For ε_{cc}, DNN again outperformed other models with an $R^2 = 0.9646$, showing its ability to explain over 96 % of the variance in the dataset. The Random Forest Regression (RFR) model also performed well, achieving $R^2 = 0.9547$ for P_{cu} and $R^2 = 0.9027$ for ε_{cc}. In contrast, traditional models including LR and SVR showed significantly lower R^2 values, particularly for ε_{cc}, where LR achieved only $R^2 = 0.5511$ and SVR achieved $R^2 = 0.2566$.

The RMSE values further highlight the superior performance of DNN and GBR. For P_{cu}, DNN achieved the lowest RMSE of 85.25 kN, closely followed by GBR with 87.85 kN. Similarly, for ε_{cc}, DNN achieved an RMSE of 0.0022 mm/mm, outperforming GBR (0.0030 mm/mm) and RFR (0.0038 mm/mm). In terms of MAE, the DNN model consistently exhibited the lowest errors, reflecting its ability to closely approximate the actual values with minimal deviation.

MAPE values also corroborate the superior performance of DNN, achieving only 3.20 % for P_{cu} and 6.92 % for ε_{cc} as shown in Fig. 20. These values indicate that DNN provides highly accurate predictions, particularly compared to LR and SVR, which demonstrated significantly higher MAPE values.

Fig. 21 compares the actual and predicted values of P_{cu} and ε_{cc} for all models. The DNN and GBR models show data points closely aligned with the diagonal line, indicating near-perfect predictions. By contrast, LR and SVR models exhibit more scatter, especially for ε_{cc}, reflecting their limited ability to handle complex, non-linear relationships.

The residual plots in Fig. 22 further illustrate the predictive accuracy of each model. For P_{cu}, DNN and GBR demonstrate minimal residuals, indicating better fitting of the data. Conversely, SVR and LR exhibit

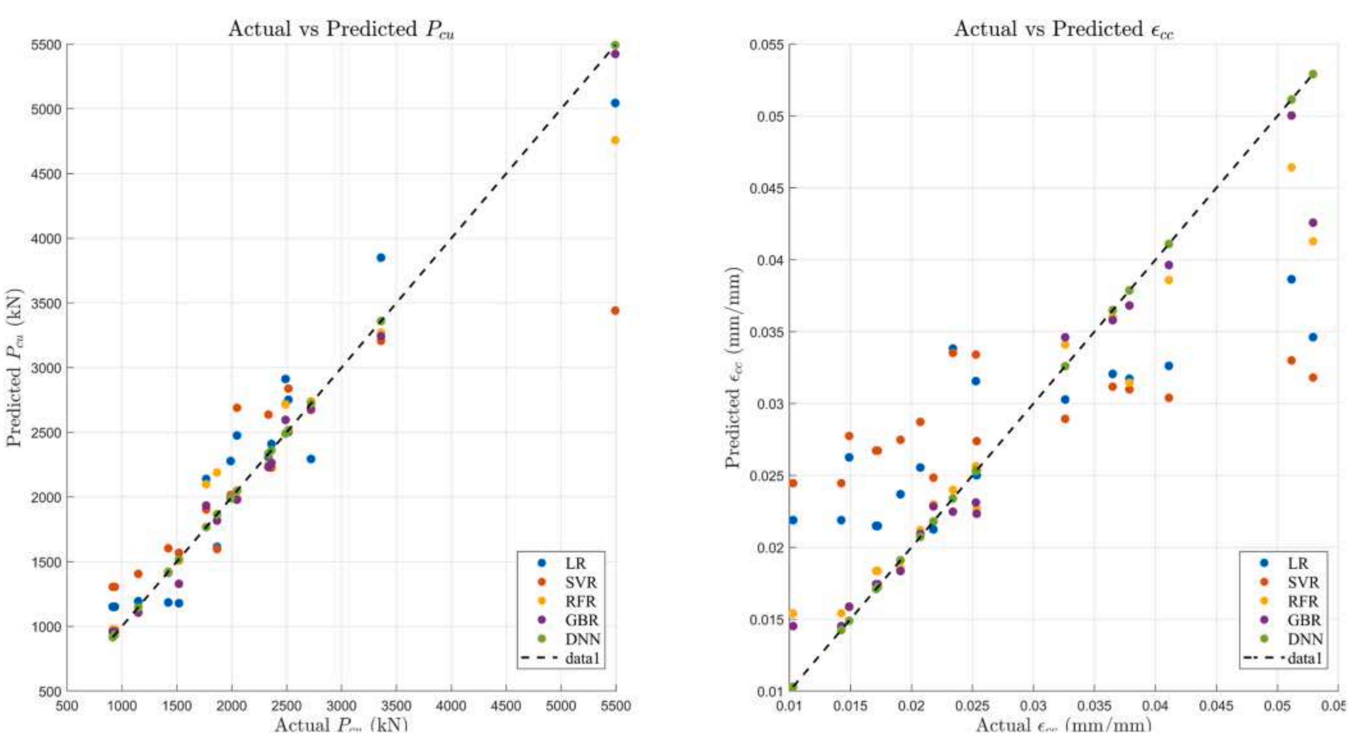

Fig. 21. Actual versus models predicted P_{cu} and ε_{cc}.

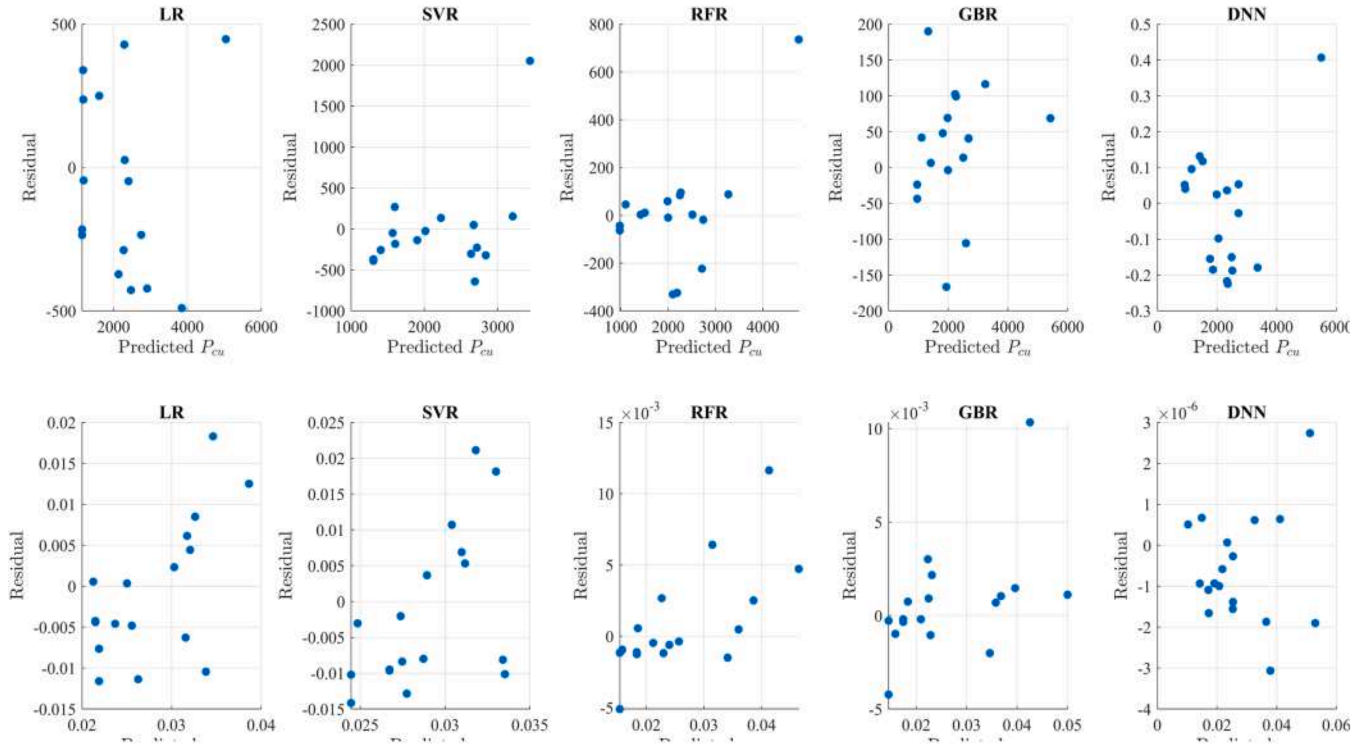

Fig. 22. Predicted P_{cu} and ε_{cc} versus residual error.

larger and more dispersed residuals, particularly at higher values, suggesting underfitting in these regions. Similarly, for ε_{cc}, DNN shows the most consistent residuals close to zero, while LR and SVR suffer from higher variance, further emphasizing their limitations.

The DNN model demonstrated the most robust performance across all metrics, owing to its capability to model highly non-linear and complex relationships inherent in the dataset. The GBR model also exhibited strong performance, likely due to its ability to handle feature interactions and capture hierarchical relationships effectively. RFR, while slightly less accurate than DNN and GBR, still provided reliable predictions, particularly for ε_{cc}.

Traditional models such as LR and SVR were unable to achieve comparable performance, particularly for ε_{cc}, due to their limitations in capturing non-linearity. The high RMSE and low R^2 values for these models highlight their inadequacy in scenarios with complex variable dependencies.

The Taylor diagrams in Fig. 23 **(A)** and **(B)** offer a comprehensive visualization of model performance for P_{cu} and ε_{cc}, respectively. These diagrams plot the standard deviation, correlation coefficient, and root-mean-squared deviation (RMSD) for each model relative to a reference dataset. The placement of models on these diagrams provides valuable insights into their predictive capabilities.

In Fig. 23 **(A)**, which assesses the models for P_{cu}, the DNN model shows the closest alignment with the reference point, exhibiting the highest correlation coefficient (approaching 0.99) and a standard deviation nearly identical to the reference. This indicates that the DNN model not only captures the variability in P_{cu} accurately but also aligns closely with the observed data. GBR follows closely, with slightly higher deviations and a marginally lower correlation coefficient, while RFR demonstrates robust performance as well. However, SVR and LR models are positioned further from the reference, reflecting their comparatively lower accuracy and limited ability to capture data variability.

In Fig. 23 **(B)**, evaluating the models for ε_{cc}, a similar trend is observed. The DNN model again exhibits the highest performance, with a correlation coefficient nearing 0.99 and minimal standard deviation discrepancies. GBR maintains strong alignment, followed by RFR, which performs reasonably well but shows slightly larger deviations. The LR and SVR models are once more positioned farther from the reference, highlighting their inability to model the complexities of strain capacity predictions effectively.

In conclusion, the results underscore the efficacy of advanced machine learning models like DNN and GBR for predicting structural parameters such as P_{cu} and ε_{cc}. These models provide superior accuracy, making them valuable tools for structural engineering applications where precise predictions are essential.

5.5.2. *Feature importance analysis results*

Feature importance analysis was conducted using SHAP (SHapley Additive exPlanations) values to understand the contribution of input variables to the predictions of P_{cu} and ε_{cc}. Figs. 24–27 present the SHAP value distributions for the GBR and RFR models for both output variables.

Figs. 24 and 25 show the SHAP value distribution for P_{cu} predictions by the GBR and RFR models, respectively. These plots indicate that A_c and t_f are the most influential variables in predicting P_{cu}. The positive SHAP values associated with larger A_c and t_f values highlight their direct contribution to increasing the load-carrying capacity of the column. Additionally, $f_c^{'}$ also demonstrated a significant positive impact, albeit less prominent than A_c and t_f.

Interestingly, f_y and E_f showed mixed contributions with both positive and negative SHAP values depending on their ranges. For instance, higher E_f values tended to have a slight negative impact on P_{cu}, which could be attributed to reduced ductility in configurations with overly stiff FRP layers. This detailed behavior suggests that the interplay between variables like t_f and E_f needs to be carefully considered during design optimization.

Figs. 26 and 27 illustrate the SHAP value distribution for ε_{cc} predictions by the GBR and RFR models, respectively. Unlike P_{cu}, the dominant contributors to ε_{cc} predictions were t_f and E_f, emphasizing the importance of FRP properties in determining the strain capacity of confined columns. Notably, larger t_f values consistently exhibited positive SHAP values, indicating their strong influence on enhancing the

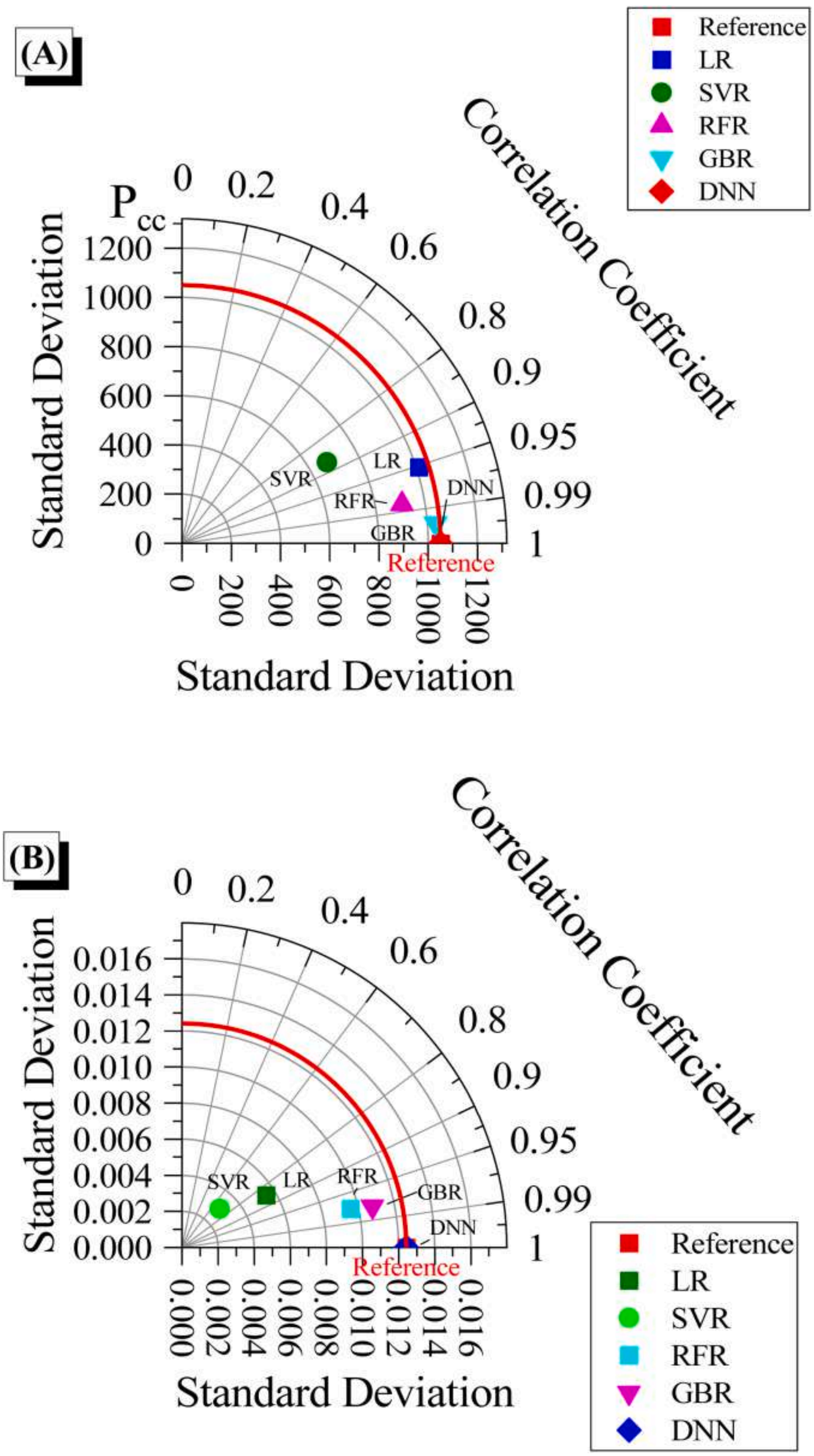

Fig. 23. Taylor diagram of model's performance to predict (A). P_{cu} and (B). ε_{cc}.

ultimate strain capacity.

On the other hand, A_s showed a significant negative impact on ε_{cc}. This could be explained by the fact that increasing the steel tube area might reduce the ductility of the system, thus lowering the strain capacity. Similarly, higher f_c' values also tended to suppress strain capacity, as concrete with higher compressive strength generally exhibits reduced deformability.

Key observations from the SHAP analysis includes:

1. **Dominant Features:**

o For P_{cu}, A_c and t_f were the most influential features across all models, reflecting the critical role of concrete area and FRP thickness in enhancing load-carrying capacity.

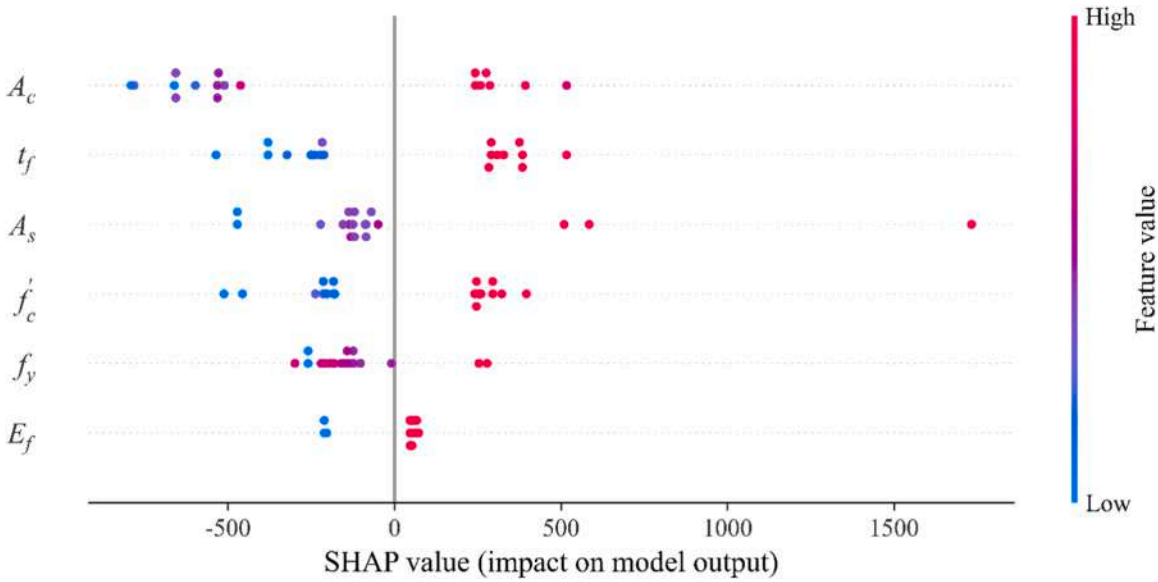

Fig. 24. SHAP value distribution for P_{cu} predictions using GBR.

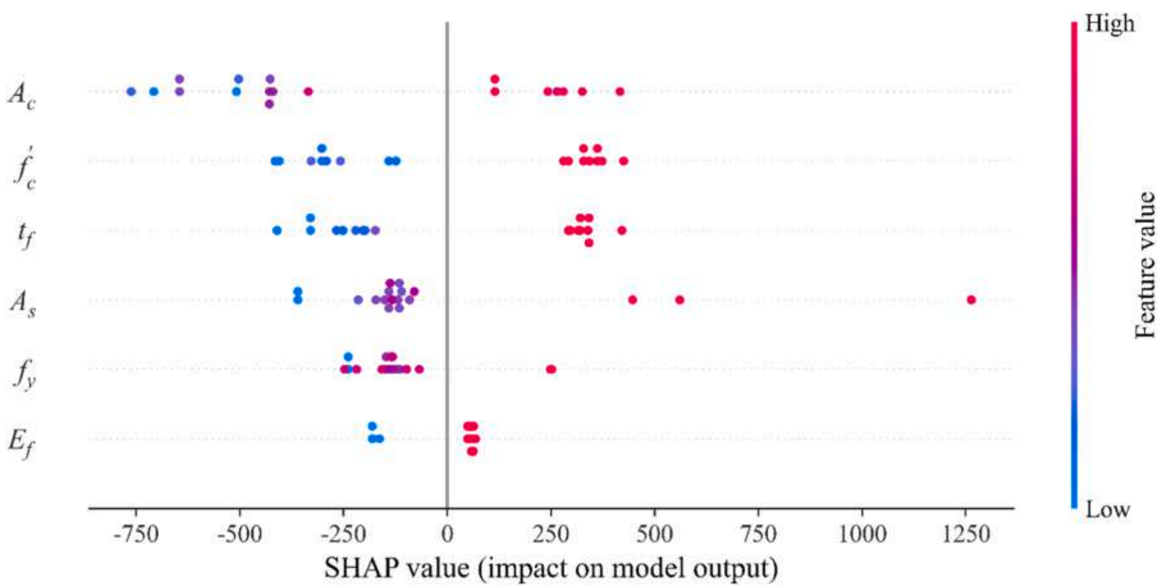

Fig. 25. SHAP value distribution for P_{cu} predictions using RFR.

- o For ε_{cc}, t_f and E_f emerged as the dominant factors, underlining the importance of FRP material properties in strain capacity predictions.

2. **Interplay of Features**:

- o The interplay between E_f and t_f is significant in both P_{cu} and ε_{cc}, as overly stiff FRP configurations (E_f) can counteract the positive effects of increased FRP thickness (t_f).
- o Similarly, the relationship between A_s and f_y highlights trade-offs between strength and ductility in hybrid concrete-steel systems.

3. **Model-Specific Observations**:

- o GBR consistently assigned higher importance to A_c and t_f, while RFR distributed importance more evenly across variables, potentially reflecting its less hierarchical structure.

5.5.3. *Graphical user interface*

To facilitate the practical implementation of the developed ML models for predicting P_{cu} and ε_{cc}, a user-friendly GUI has been developed and is hosted on GitHub at SDSTC Prediction GUI Repository. This GUI provides engineers, researchers, and practitioners with a streamlined platform to leverage the predictive capabilities of the machine learning models without requiring in-depth programming expertise.

The GUI, as shown in Fig. 28, allows users to input structural and material parameters related to FRP-confined columns.

Once these values are entered, users can click the "Predict" button to generate predictions for P_{cu} and ε_{cc}. The results are displayed in an intuitive pop-up dialog box for immediate reference, ensuring quick accessibility to key structural predictions. For instance, in the screenshot depicted in Fig. 28, the GUI predicts P_{cu} of 2921.65 kN and ε_{cc} of 0.02292 mm/mm based on the provided input parameters.

The GUI is designed with simplicity and efficiency in mind. It uses a clean, minimalistic layout where each parameter is clearly labeled, ensuring that users can accurately input data without ambiguity. The

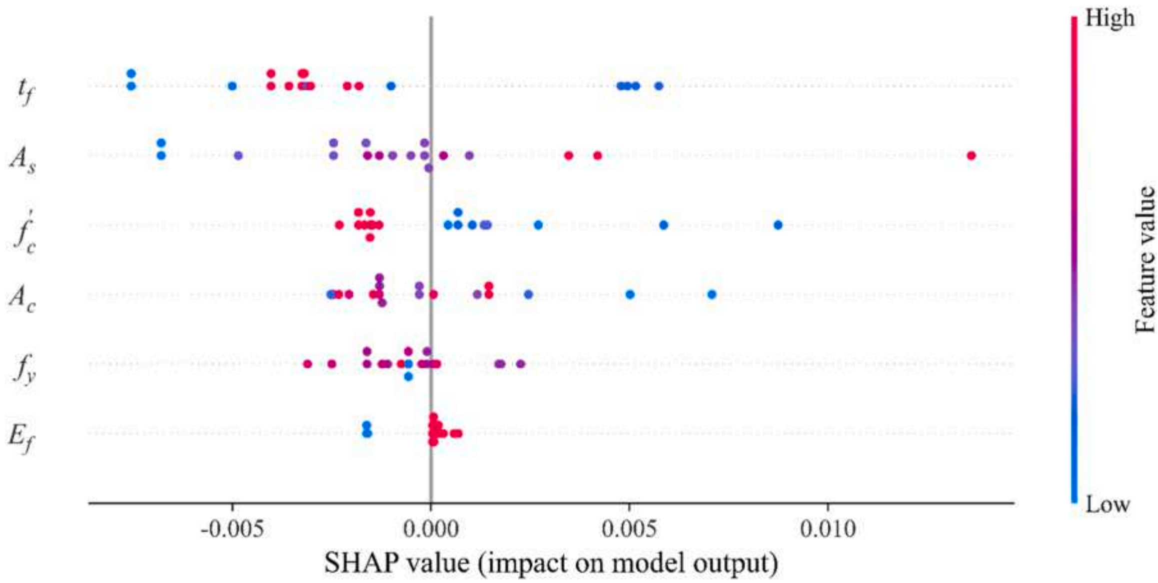

Fig. 26. SHAP value distribution for ε_{cc} predictions using GBR.

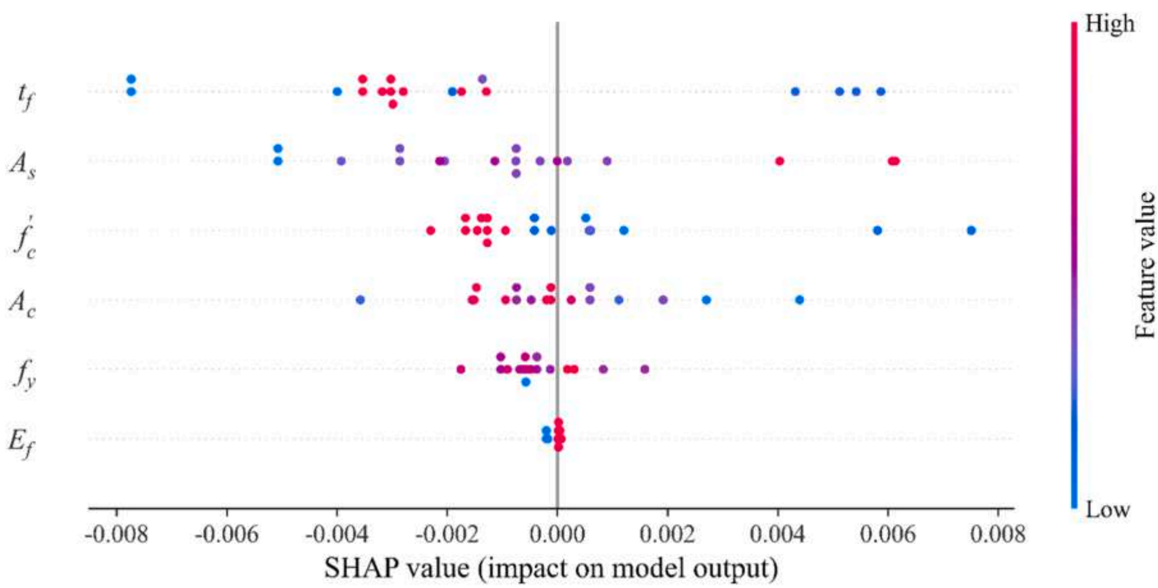

Fig. 27. SHAP value distribution for ε_{cc} predictions using RFR.

interface is lightweight and responsive, making it accessible even on systems with limited computational resources. Furthermore, the use of descriptive labels and intuitive functionality reduces the learning curve, making the tool accessible to a wide range of users, from students to experienced engineers.

The GUI is implemented using Python, leveraging libraries such as Tkinter for interface design and backend integration with the trained ML models. The hosting on GitHub provides easy access to the source code and instructions for deployment, enabling users to download, install, and customize the GUI as needed. Additionally, the open-source nature of the repository encourages collaboration and future enhancements by the community.

This GUI serves as a valuable tool in structural engineering design and analysis. By providing immediate predictions of key structural metrics, it enables engineers to:

- Evaluate different design configurations during preliminary design stages.
- Optimize material usage for cost-efficiency and performance.
- Perform rapid sensitivity analyses by varying input parameters and observing their effects on P_{cu} and ε_{cc}.

5.5.4. Limitations and future directions

While the findings of this study provide valuable insights into the prediction of P_{cu} and ε_{cc} using advanced ML models, several limitations need to be acknowledged. Addressing these limitations can pave the way for future improvements and novel research directions.

Limitations

1. **Dataset Size and Diversity**: Despite efforts to compile a robust dataset, the sample size (N = 116) is relatively small, potentially limiting the generalizability of the models. Furthermore, the dataset may lack sufficient diversity in terms of material properties, geometries, and boundary conditions. For example, variations in environmental factors, such as temperature or sustained loading, were not explicitly included, which could impact real-world applicability.

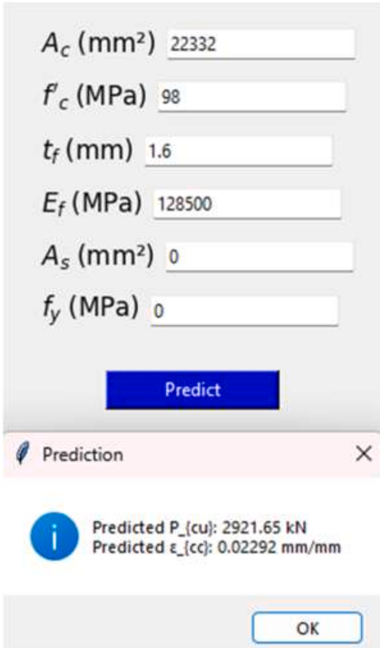

Fig. 28. Screenshot of graphical user interface.

2. **Model Interpretability**: Although SHAP values were used to interpret feature contributions, the inherent complexity of DNN and ensemble models including GBR and RFR poses challenges for full interpretability. Engineering practitioners may find it difficult to directly link the model's predictions to physical phenomena without extensive additional analyses.
3. **Computational Complexity**: The DNN model, while highly accurate, requires significant computational resources for training and hyperparameter tuning. This limitation might restrict its deployment in scenarios where computational efficiency is critical, such as real-time structural health monitoring or rapid preliminary design assessments.
4. **Exclusion of Long-term and Cyclic Loading Effects**: The current models focus exclusively on monotonic loading conditions. However, many real-world applications, such as seismic or wind-exposed structures, involve cyclic loading and long-term environmental degradation, which were not considered in this study.
5. **Simplified Feature Interactions**: The dataset and models did not account for complex interdependencies between input features beyond those captured by statistical relationships. For instance, interactions between FRP properties (t_f, E_f) and concrete parameters ($f_c^{'}$) under extreme stress states may exhibit nonlinear behavior that the current dataset does not adequately reflect.

Future directions

1. **Expanding the Dataset**: Future studies should focus on increasing the dataset size by incorporating additional experimental and numerical data. Expanding the diversity of material properties, column geometries, and loading scenarios will enhance the robustness and generalizability of the models. Including data on cyclic loading, fire exposure, and long-term environmental effects will also provide a more comprehensive basis for predictions.
2. **Developing Physics-Informed Machine Learning Models**: Integrating domain knowledge into ML models can bridge the gap between data-driven predictions and physical understanding. Physics-informed neural networks (PINNs) or hybrid models combining finite element analysis with ML could improve both accuracy and interpretability.
3. **Enhancing Model Interpretability**: Future work should focus on developing interpretable ML models or techniques that can provide more explicit physical explanations for predictions. Leveraging advanced explainability frameworks or simpler, physics-guided surrogate models could make these tools more accessible to engineering practitioners.
4. **Improving Computational Efficiency**: To make DNN and other high-performing models more practical for real-time applications, efforts should be directed toward optimizing their architectures for efficiency. Techniques such as model pruning, quantization, and transfer learning can reduce computational requirements without compromising accuracy.
5. **Incorporating Multimodal Data**: Integrating data from diverse sources, such as experimental measurements, sensor outputs, and field observations, can enhance the richness of the training data. For instance, combining visual inspections, acoustic emissions, and load-displacement data could improve predictions and reliability.
6. **Extending to Broader Structural Applications**: While this study focused on FRP-confined columns, the methodologies developed here can be extended to other structural components and systems, such as beams, slabs, and hybrid materials. Exploring these extensions will broaden the applicability of the findings.

6. Conclusion

Based on comprehensive numerical and machine learning modeling conducted on square double-skin tubular columns (SDSTC), the following conclusions were drawn in this study.

- Enhancing the yield strength of steel in DSTC specimens to 667.5 MPa increases ultimate axial load but results in varied strain responses: single tubes show significant strain variability due to reduced ductility from higher carbon content, while double tubes exhibit minor strain improvements, suggesting minimal ductility gain with an extra tube.
- Adding GFRP layers to circular hollow DSTC specifications enhances ultimate axial load and strain, with diminishing returns beyond three layers. For smaller diameters (76.3 mm), load increases marginally after three layers, while strain significantly improves up to 150.3 % for four layers. In larger diameters (114.5 mm), load and strain gains are more modest, suggesting size affects the efficiency of GFRP layer additions in improving structural properties.
- DSTC research reveals that hollow specimens with circular tubes surpass square ones in load capacity (10 %-16 %) and ductility (45 %-55 %). Conversely, concrete-filled specimens show square tubes outperforming circular ones in load resistance (4.6 %-6.3 %) with less pronounced ductility differences. The impact of tube shape on performance varies with concrete strength, indicating material and geometric configurations significantly influence DSTC structural behavior.
- The use of dual steel tubes in DSTC specimens significantly increases ultimate axial load capacity (22.3 %-45.6 %) and ultimate strain (51.8 %-118.3 %), indicating enhanced strength and ductility compared to single-tube configurations. This improvement is attributed to steel's superior material properties over concrete.
- In DSTC specimens, increasing steel tube size and thickness decreases ultimate axial load capacity in hollow sections but increases it in filled sections by up to 30 %, reflecting steel's higher strength. Hollow sections show enhanced ductility with larger steel dimensions, while filled sections exhibit variable strain responses. Strength gains in filled sections are significant, reaching up to 80 % in certain groups, with double-tube configurations also showing notable strength increases but varied strain outcomes.
- The machine learning models demonstrated robust performance across all training and testing phases. The DNN model outperformed other models, achieving exceptional predictive accuracy for both P_{cu}

and ε_{cc}. Specifically, the DNN model achieved R^2 values of 0.997 and 0.965 for P_{cu} and ε_{cc}, respectively, with corresponding RMSE values of 85.25 kN and 0.0022 mm/mm. These results indicate that the DNN model provides highly accurate predictions, outperforming traditional models such as linear regression, support vector regression, random forest regression, and gradient boosting regression. This demonstrates the efficacy of advanced machine learning techniques in capturing the complex nonlinear behavior of DSTC specimens and highlights their potential for future engineering applications.

The present study has analyzed the impact of a limited set of variables, such as the concrete's area and strength, the thickness and elastic modulus of FRP wrapping layers, and the thickness and yield strength of the steel tube. Future research should aim to include factors like the specimen's size, slenderness ratio, loading conditions (e.g., eccentric or cyclic loading), FRP material types (PEN, PET, CFRP, etc.), and the aspect ratio of rectangular cross-sections.

Declaration of Competing Interest

The authors declares that they have no known competing financial interests or personal relationship that could have appeared to the work reported in this paper.

References

[1] Prishchepa OS, Karavaev AV, Bushinskaya AV. Resilience of high-rise RC buildings to dynamic impacts. IOP Conf Ser: Mater Sci Eng 2017;262:012057. https://doi.org/10.1088/1757-899x/262/1/012057.
[2] Sarkisian M, Lee P, Gordon J, Garai R. Designing resilient structures subjected to abnormal loads. : AEI 2015 2015:331–41.
[3] Lu X, Chen A. Quantitative evaluation and improvement of seismic resilience of a tall frame shear wall structure. Struct Des Tall Spec Build 2021;31. https://doi.org/10.1002/tal.1899.
[4] Ozbakkaloglu T. Reflections on mechanisms affecting the behavior of FRP-concrete-steel double-skin tubular columns. Key Eng Mater 2016;705:323–31. https://doi.org/10.4028/www.scientific.net/KEM.705.323.
[5] Xiong M, Lan Z, Chen G, Lu Y, Xu Z. Behavior of FRP-HSC-steel tubular columns under axial compression: a comparative study. Compos Struct 2021;261:113566. https://doi.org/10.1016/J.COMPSTRUCT.2021.113566.
[6] Fanggi BAL, Ozbakkaloglu T. Influence of inner steel tube properties on compressive behavior of FRP-HSC-steel double-skin tubular columns. Appl Mech Mater 2013;438-439:701–5. https://doi.org/10.4028/www.scientific.net/amm.438-439.701.
[7] Louk Fanggi BA, Ozbakkaloglu T. Effect of loading pattern on performance of FRP-HSC-steel double skin tubular columns. Adv Mater Res 2014;919-921:83–7. https://doi.org/10.4028/www.scientific.net/amr.919-921.83.
[8] Farahi M, Heidarpour A, Zhao X, Al-Mahaidi R. Compressive behaviour of concrete-filled double-skin sections consisting of corrugated plates. Eng Struct 2016;111:467–77. https://doi.org/10.1016/J.ENGSTRUCT.2015.12.012.
[9] Wan J, Wang C, Liang J, Lin S. Axial compression performance of concrete filled double skin (SHS outer and CHS inner) steel tubular columns strengthened by CFRP. Adv Struct Eng 2023. https://doi.org/10.1177/13694332231161109.
[10] Huang X, Su S, Xu Z, Miao Q, Li W, Wang L. Advanced composite materials for structure strengthening and resilience improvement. Buildings 2023;13:2406. https://doi.org/10.3390/buildings13102406.
[11] Zou Q, Xu C, Dong Z, Wu D, An X. Deformation behavior of carbon Fiber/Al composites with corrugated structure for developing the rolling plate. Adv Eng Mater 2023;25. https://doi.org/10.1002/adem.202300503.
[12] Zuki S, Jayaprakash J, Shahidan S, Yong O. Behavior of fire exposed concrete-filled double skin steel tubular (CFDST) columns under concentric axial loads. Appl Mech Mater 2015;773-774:938–42. https://doi.org/10.4028/www.scientific.net/AMM.773-774.938.
[13] Zhang B, Teng J, Yu T. Experimental behavior of hybrid FRP-concrete-steel double-skin tubular columns under combined axial compression and cyclic lateral loading. Eng Struct 2015;99:214–31. https://doi.org/10.1016/J.ENGSTRUCT.2015.05.002.
[14] Dwaikat MB, Kodur VKR. Response of restrained concrete beams under design fire exposure. J Struct Eng 2009;135:1408–17. https://doi.org/10.1061/(asce)st.1943-541x.0000058.
[15] Hashemi A, Zarnani P, Masoudnia R, Quenneville P. Seismic resilient lateral load resisting system for timber structures. Constr Build Mater 2017;149:432–43. https://doi.org/10.1016/j.conbuildmat.2017.05.112.
[16] Patel V, Liang Q, Hadi M. Numerical analysis of circular double-skin concrete-filled stainless steel tubular short columns under axial loading. Structures 2020;24:754–65. https://doi.org/10.1016/j.istruc.2020.02.001.
[17] Liang Q. Numerical simulation of high strength circular double-skin concrete-filled steel tubular slender columns. Eng Struct 2018. https://doi.org/10.1016/J.ENGSTRUCT.2018.04.062.
[18] Elchalakani M, Patel V, Karrech A, Hassanein M, Fawzia S, Yang B. Finite element simulation of circular short CFDST columns under axial compression. Structures 2019. https://doi.org/10.1016/J.ISTRUC.2019.06.004.
[19] Ahmed M, Ci J, Yan X, Lin S, Chen S. Numerical modeling of axially loaded circular concrete-filled double-skin steel tubular short columns incorporating a new concrete confinement model. Structures 2021;30:611–27. https://doi.org/10.1016/J.ISTRUC.2021.01.044.
[20] Youssf O, Hassanli R, Mills J, Zhuge Y. Axial compression behaviour of hybrid double-skin tubular columns filled with rubcrete. J Compos Sci 2019. https://doi.org/10.3390/JCS3020062.
[21] Ali H, Salman W. Effect of void ratio of inner steel tube on compression behavior of double skin tubular column. IOP Conf Ser: Mater Sci Eng 2019;584. https://doi.org/10.1088/1757-899X/584/1/012027.
[22] Le T, Patel V, Liang Q, Huynh P. Numerical modeling of rectangular concrete-filled double-skin steel tubular columns with outer stainless-steel skin. J Constr Steel Res 2021;179:106504. https://doi.org/10.1016/J.JCSR.2020.106504.
[23] Li P, Hu J, Xing F, Sui L, Zhou Y, Chen C. Behavior and modeling of double-skin tubular columns filled by ultra-lightweight cement composites (ULCCs). Compos Struct 2021;263:113709. https://doi.org/10.1016/J.COMPSTRUCT.2021.113709.
[24] Chen J, Wang J, Xie F, Duan A. Behavior of thin-walled dodecagonal section double skin concrete-filled steel tubular beam-columns. Thin-Walled Struct 2016;104:135–43. https://doi.org/10.1016/J.TWS.2016.03.008.
[25] Guo Z, Chen Y, Wang Y, Jiang M. Experimental study on square concrete-filled double skin steel tubular short columns. Thin-Walled Struct 2020;156:107017. https://doi.org/10.1016/j.tws.2020.107017.
[26] Kim HJ, Kim HY, Yeo IH. An Experimental Study on the Fire Behavior of CFT Columns under the Constant Axial Loading Condition in Fire. Adv Mater Res 2012;446-449:1298–306. https://doi.org/10.4028/www.scientific.net/amr.446-449.1298.
[27] Ding F, Wang W, Lu D, Liu X. Study on the behavior of concrete-filled square double-skin steel tubular stub columns under axial loading. Structures 2020;23:665–76. https://doi.org/10.1016/j.istruc.2019.12.008.
[28] Fan S, He T, Li W, Zeng C, Chen P, Chen L, Shu J. Machine learning-based classification of quality grades for concrete vibration behaviour. –105694 Autom Constr 2024;167:105694. https://doi.org/10.1016/j.autcon.2024.105694.
[29] Shu J, Zhang X, Li W, Zeng Z, Zhang H, Duan Y. Point cloud and machine learning-based automated recognition and measurement of corrugated pipes and rebars for large precast concrete beams. –105493 Autom Constr 2024;165:105493. https://doi.org/10.1016/j.autcon.2024.105493.
[30] Deng J, Wu R, Sun Z, Qian D, Zhang Y. A prediction model of ultimate forming dimension for profile ring with outer groove in ring rolling process. Int J Adv Manuf Technol 2023;130:491–510. https://doi.org/10.1007/s00170-023-12528-1.
[31] Ali L, Isleem HF, Bahrami A, Jha I, Zou G, Kumar R, Sadeq AM, Jahami A. Integrated behavioural analysis of FRP-confined circular columns using FEM and machine learning. –100444 Compos Part C: Open Access 2024:100444. https://doi.org/10.1016/j.jcomc.2024.100444.
[32] Isleem HF, Zewudie BBefikadu, Bahrami A, Kumar R, Xingchong W, Samui P. Parametric investigation of rectangular CFRP-confined concrete columns reinforced by inner elliptical steel tubes using finite element and machine learning models. –e23666 Heliyon 2023;10:e23666. https://doi.org/10.1016/j.heliyon.2023.e23666.
[33] Isleem HF, Naga A, Bahrami R, Kumar N, Hamah Sor. Nonlinear finite element and machine learning modeling of tubed reinforced concrete columns under eccentric axial compression loading. Alex Eng J /Alex Eng J 2024;92:380–416. https://doi.org/10.1016/j.aej.2024.02.026.
[34] Hong Z, Wang W, Zheng L, Shi Y-L. Machine learning models for predicting axial compressive capacity of circular CFDST columns. –105285 Structures 2023;57:105285. https://doi.org/10.1016/j.istruc.2023.105285.
[35] Nguyen H, Vu T, Vo TP, Thai H-T. Efficient machine learning models for prediction of concrete strengths. Constr Build Mater 2021;266:120950. https://doi.org/10.1016/j.conbuildmat.2020.120950.
[36] Stergiou K, Ntakolia C, Varytis P, Koumoulos EP, Karlsson P, Moustakidis Serafeim. Enhancing property prediction and process optimization in building materials through machine learning: a review. –112031 Comput Mater Sci 2023;220:112031. https://doi.org/10.1016/j.commatsci.2023.112031.
[37] Nguyen T, Ly H. Predicting axial compression capacity of CFDST columns and design optimization using advanced machine learning techniques. –105724 Structures 2024;59:105724. https://doi.org/10.1016/j.istruc.2023.105724.
[38] Wu B, Dang S, Zhu YF, Yao Y. A machine learning based interaction model to predict robustness of concrete-filled double skin steel tubular columns under fire condition. –105332 Structures 2023;57:105332. https://doi.org/10.1016/j.istruc.2023.105332.
[39] Louk Fanggi BA, Ozbakkaloglu T. Square FRP–HSC–steel composite columns: Behavior under axial compression. Eng Struct 2015;92:156–71. https://doi.org/10.1016/j.engstruct.2015.03.005.
[40] Yu T, Teng J. Behavior of hybrid FRP-concrete-steel double-skin tubular columns with a square outer tube and a circular inner tube subjected to axial compression. J Compos Constr 2013;17(2):271–9. https://doi.org/10.1061/(asce)cc.1943-5614.0000331.
[41] Mushthofa M, Nurfauzi FP, Hardawati A. Investigation of effective section reduction in low carbon steel during SMAW welding. Tek: J Ilm Fak Tek Sipil Dan

Perenc Univ Islam Indones Yogyak 2023;28(2):79–89. https://doi.org/10.20885/teknisia.vol28.iss2.art2.

[42] Bongioví G, Siccinio M, Spagnuolo GA, Catanzaro I, Chiovaro P, Di Maio PA, Vallone E. Thermal and structural analysis of the European water-cooled lithium lead breeding blanket concept in the L-H mode transition. –114137 Fusion Eng Des 2024;199:114137. https://doi.org/10.1016/j.fusengdes.2023.114137.

[43] Xie Q, Xu Q, Xiu Z, Liu L, Du X, Jianghui Y, Liu F. Convenient method for large-deformation finite-element simulation of submarine landslides considering shear softening and rate correlation effects. –81 J Mar Sci Eng 2023;12(1):81. https://doi.org/10.3390/jmse12010081.

[44] Zhang Q, Hu L, Gao X. Fatigue life prediction of steel spiral cases in pumped-storage power plants: factors to be considered. –107908 Eng Fail Anal 2024;157:107908. https://doi.org/10.1016/j.engfailanal.2023.107908.

[45] Abramowicz M, Chybiński M, Polus Ł, Wróblewski T. Free Vibrations of Sustainable Laminated Veneer Lumber Slabs. Sustainability 2023;16(1):166. https://doi.org/10.3390/su16010166. 166.

[46] Tola SG. Numerical investigation of seismic performance of reinforced concrete frame strengthened with CFRP. Eng Appl Sci 2023;8(5). https://doi.org/10.11648/j.eas.20230805.12.

[47] Al Rawi Y, Temsah Y, Ghanem H, Jahami A, Elani M. The effect of impact loads on prestressed concrete slabs. Proc Int Struct Eng Constr 2018;5(1). https://doi.org/10.14455/isec.res.2018.54.

[48] Elani M, Temsah Y, Ghanem H, Jahami A, Al Rawi Y. The effect of shear reinforcement ratio on prestressed concrete beams subjected to impact load. Proc Int Struct Eng Constr 2018;5(1). https://doi.org/10.14455/isec.res.2018.55.